Evolution of rift systems and their fault networks in response to surface processes

Derek Neuharth[1,2], Sascha Brune[1,2], Thilo Wrona[1], Anne Glerum[1], Jean Braun[1,2], Xiaoping Yuan[3,1]

[1]GFZ German Research Centre for Geosciences, Telegrafenberg, 14473 Potsdam, Germany.

[2]Institute of Geosciences, University of Potsdam, Germany.

[3]School of Earth Sciences, China University of Geosciences, Wuhan, China

Corresponding author: Derek Neuharth (djneuh@gfz-potsdam.de)

Key Points:

- We apply a new fault analysis toolbox to coupled numerical models of tectonics and surface processes.
- Fault network evolution of the major symmetric, asymmetric, narrow and wide rift types can be described in five distinct phases.
- Surface processes reduce fault network complexity and delay breakup by enhancing strain localization and increasing fault longevity.

Abstract

Continental rifting is responsible for the generation of major sedimentary basins, both during rift inception and during the formation of rifted continental margins. Geophysical and field studies revealed that rifts feature complex networks of normal faults but the factors controlling fault network properties and their evolution are still matter of debate. Here, we employ high-resolution 2D geodynamic models (ASPECT) including two-way coupling to a surface processes code (FastScape) to conduct 12 models of major rift types that are exposed to various degrees of erosion and sedimentation. We further present a novel quantitative fault analysis toolbox (Fatbox), which allows us to isolate fault growth patterns, the number of faults, and their length and displacement throughout rift history. Our analysis reveals that rift fault networks may evolve through five major phases: 1) distributed deformation and coalescence, 2) fault system growth, 3) fault system decline and basinward localization, 4) rift migration, and 5) breakup. These phases can be correlated to distinct rifted margin domains. Models of asymmetric rifting suggest rift migration is facilitated through both ductile and brittle deformation within a weak exhumation channel that rotates subhorizontally and remains active at low angles. In sedimentation-starved settings, this channel satisfies the conditions for serpentinization. We find that surface processes are not only able to enhance strain localization and to increase fault longevity but that they also reduce the total length of the fault system, prolong rift phases and delay continental breakup.

1 Introduction

Rift-related thinning of the crust generates major depressions that are often filled with sediments. These sedimentary basins may provide a range of georesources such as geothermally exploitable hot aquifers (Jolie et al., 2021), ore deposits (Wilkinson, 2014), or perhaps even natural hydrogen (Lefeuvre et al., 2021). Our understanding of the processes that shape rifts, rifted margins, and their sedimentary basins is however inhibited among others by three challenges: (1) the cross-scale nature of deformation processes, (2) the interaction between faults and surface processes, (3) the interplay between complex mechanisms that facilitate rift migration. In the next paragraphs we describe these challenges by summarizing the current knowledge and its limits.

Rifting is an inherently cross-scale process. Normal faults that accommodate most of the extension in many rifts worldwide feature a width ranging from several centimeters to tens of meters (Scholz, 2019). Spacing in-between major normal faults can vary from 1 km (Muirhead et al., 2016) up to a few tens of kilometers (Whitmarsh et al., 2001). The extending lithosphere, however, is typically hundreds of kilometers thick. Bridging these scales by means of geodynamic modelling tools remains a major challenge, even if fault localization processes are parameterized and if additional processes like melt generation and diking are neglected. Recent advances in computational techniques allowed for a steadily growing resolution of numerical rift models that lead to insights on rift migration processes (Brune et al., 2014), deformation phases (Naliboff et al., 2017), and fault-related unconformities (Pérez-Gussinyé et al., 2020). But deducing the evolution of variables that describe the kinematics of discrete faults like instantaneous slip rate, cumulative displacement or the number of active faults has remained very difficult in lithospheric-scale models so far.

One of the key factors shaping rift and rifted margin architectures are surface processes (e.g. Gawthorpe and Leeder, 2000; Clerc et al., 2018). Topographic erosion and sediment deposition modify Earth's surface through time, changing upper crustal temperatures and affecting crustal pressure conditions through sediment loads (e.g., Olive et al., 2014). The change in loading is an important factor for the evolution of individual faults, where mass redistribution from the uplifted and eroding footwall to the subsiding depositional hanging wall aids strain localization (Maniatis et al., 2009) and prolongs fault activity (Andrés-Martínez et al., 2019; Theunissen and Huismans, 2019; Beucher and Huismans, 2020). Similarly, sedimentation promotes rift migration by enhancing hyperextension of the crust and possibly delays continental breakup (Buiter, 2021). Previous studies have used 2D numerical models to investigate the interplay between surface processes and rift evolution (Andrés-Martínez et al., 2019; Theunissen and Huismans, 2019; Beucher and Huismans, 2020; Pérez-Gussinyé et al., 2020). These studies take a qualitative look at changes to rift system evolution, but do not quantitatively analyze variations in fault properties over time. Three-dimensional analog models suggest that surface processes do not have a large effect on overall rift evolution, but do affect the internal structure of rifts and produce more realistic rift geometries (Zwaan et al., 2018). These points highlight the importance of a quantitative fault analysis to understand the geometry and kinematics of fault networks, and how they evolve for varying degrees of surface process efficiency.

Previous numerical studies have shown a striking similarity in rift evolution when modeling rift migration, crustal hyper-extension and the formation of asymmetric rifted margins (Brune et al., 2014; Jammes and Lavier, 2016; Tetreault and Buiter, 2018; Pérez-Gussinyé et al., 2020). Comparing these models to concepts based on geophysical data, however, has led to discrepancies resulting in ongoing discussions on the mechanisms responsible (Lymer et al., 2019). The debate focusses on two issues: 1) Are key normal faults active at the same time (Sibuet, 1992; McDermott and Reston, 2015), or is faulting sequential such that a given fault will become extinct before a new one forms (Goldsworthy and Jackson, 2001; Ranero and Pérez-Gussinyé, 2010)? 2) Do basal detachment faults exist and slip at low angles (Reston and Pérez-Gussinyé, 2007; Lymer et al., 2019), or did they form as steeply dipping normal faults that were rotated passively similar to a rolling hinge (Buck, 1988; Choi et al., 2013)? It has been suggested that for slip to occur at low-angles weak rocks like serpentine are needed (Pérez-Gussinyé et al., 2001). Serpentinization of exhumed mantle rocks occurs in the presence of large amounts of seawater, requiring active faults within a thin portion of an entirely brittle crust (<10 km; Reston and Pérez-Gussinyé, 2007; Reston, 2010; Bayrakci et al., 2016; Muldashev et al., 2021). Assessing these factors requires both high-resolution models to determine the mechanisms that influence rift migration, and a way to quantitatively evaluate slip and activity time along discrete faults.

In this study we address three primary questions: 1) How do fault networks evolve in different rifts and rifted margins? 2) How are fault systems affected by surface processes? 3) How do detachment faults and fault sequentiality evolve during rift migration? We first describe the setup of our geodynamic model that pairs the tectonic code ASPECT with the landscape evolution code FastScape. We then introduce a new toolbox to extract discrete faults from our model results, track them through time and compute key fault properties such as the number of faults, slip, displacement, and fault length. We focus on three distinct rift settings to describe the joint evolution of fault networks and sedimentation patterns. Finally, we highlight new insights into fault sequentiality, deformation processes and serpentinization at rifted margins.

2 Methods

We use a two-way coupling between the geodynamic code ASPECT (Advanced Solver for Problems in Earth's ConvecTion; version 2.3.0-pre, commit e27f643; Kronbichler et al., 2012; Heister et al., 2017; Rose et al., 2017; Glerum et al., 2018; Gassmöller et al., 2018) and the landscape evolution model FastScape (version fastscapelib-fortran, commit 18f2588; Braun and Willett, 2013; Yuan et al., 2019a, 2019b) to simulate a 2D extensional system with erosion and sediment deposition.

2.1 Geodynamic model

The geodynamic code ASPECT assumes an extended Boussinesq approximation with an infinite Prandtl number (i.e., no inertial term) and solves the following conservation equations,

$$-\nabla \cdot (2\eta\dot{\varepsilon}) + \nabla P = \rho \boldsymbol{g}\,, \qquad (1)$$

$$\nabla \cdot \boldsymbol{u} = 0\,, \qquad (2)$$

$$\begin{aligned} \bar{\rho} C_p \left(\frac{\partial T}{\partial t} + \boldsymbol{u} \cdot \nabla T\right) - \nabla \cdot k \nabla T = {} & \bar{\rho} H \\ & + (2\eta\dot{\varepsilon}) : \dot{\varepsilon} \\ & + \alpha T\, (\boldsymbol{u} \cdot \nabla P)\,, \end{aligned} \qquad (3)$$

$$\frac{\partial c_i}{\partial t} + \boldsymbol{u} \cdot \nabla c_i = q_i\,, \qquad (4)$$

where (1) is the conservation of momentum, with the effective viscosity η, the deviator of the strain rate tensor $\dot{\varepsilon}$ (defined as $\frac{1}{2}(\nabla \boldsymbol{u} + (\nabla \boldsymbol{u})^T)$), the velocity $\boldsymbol{u}$, the pressure P, the density ρ, and $\boldsymbol{g}$ the gravity. Equation (2) describes the conservation of mass. Equation (3) is the conservation of energy, where $\bar{\rho}$ is the reference adiabatic density, C_p the specific heat capacity, T the temperature, k the thermal conductivity, H the radiogenic heating, and α the thermal expansivity. As right-hand-side heating terms, we include radioactive heating, frictional heating, and adiabatic heating from top to bottom, respectively. Finally, we solve the advection equation (4) for each compositional field c_i (e.g., upper crust, sediment age, and accumulated plastic strain), with reaction rate q_i nonzero for the plastic strain and viscous strain fields.

2.1.1 Rheology equations

The model uses a viscoplastic rheology (Glerum et al., 2018) that includes both plastic and viscous weakening. To simulate plastic weakening, the angle of friction is weakened by 75% from an initial value of 26.56° to 6.64° (corresponding to friction coefficients of 0.5 and 0.12, respectively) as plastic strain accumulates over the interval from 0 to 1. The viscous portion of the model is an averaged composite of diffusion and dislocation creep following Karato and Wu (1993; see parameter values in Table S1). Viscous weakening reduces the creep prefactors by 75% over an accumulated viscous strain interval of 0 to 1.

2.2 Landscape evolution model

FastScape changes the model surface accounting for the stream-power law (SPL) fluvial erosion, hillslope or marine diffusion, lateral advection, and vertical uplift (Braun and Willett, 2013; Yuan et al., 2019a, 2019b). These processes are described by,

$$\frac{dh}{dt} = \boldsymbol{U} \qquad for\ h \geq h_{sea} \quad (7)$$

$$- K_f A^m S^n$$

$$+ \frac{G}{A} \int_A \left(\boldsymbol{U} - \frac{dh}{dt} \right) dA$$

$$+ K_c \nabla^2 h$$

$$+ \boldsymbol{v} \cdot \nabla h\,,$$

$$\frac{dh}{dt} = K_m \nabla^2 h + Q_s + \boldsymbol{v} \cdot \nabla h\,, \quad for\ h < h_{sea} \quad (8)$$

where *h* is the topographic elevation, $\boldsymbol{U}$ the uplift rate, K_f the bedrock erodibility, *A* the drainage area, *S* the slope, *m* the drainage area exponent, *n* the slope exponent, *G* the deposition coefficient, K_c the continental diffusion coefficient, **v** the lateral velocity, K_m the marine diffusion coefficient, and Q_s the total continental sediment flux. Equation (7) represents processes in the continental domain and from top to bottom including the uplift rate, SPL fluvial erosion, sediment deposition, hillslope diffusion, and lateral advection. Equation (8) represents marine processes. In the following, we use *m* = 0.4, *n* = 1, and *G* = 1 following previous studies (Yuan et al., 2019a, 2019b; Guerit et al., 2019).

2.3 ASPECT-FastScape coupling

The two-way coupling between ASPECT and FastScape is implemented through a back-and-forth transfer of surface velocities and surface topography (see supplement, Neuharth et al., 2021). During the first timestep, ASPECT initializes and runs FastScape using the initial model surface topography and velocities from the zeroth timestep. In 2D (X-Z) ASPECT models, velocities and topographies are duplicated along the Y-direction to provide a horizontal X-Y grid of values for FastScape. FastScape uses the ASPECT values to advect/uplift the surface and further alters the surface using equations (7) and (8). After FastScape has run, the new surface is compared to the previous surface from the start of the timestep and converted to a vertical (Z) mesh velocity updating the ASPECT surface at each nodal point,

$$\boldsymbol{V}_{\boldsymbol{z}(\boldsymbol{x},\boldsymbol{y})} = \frac{h_{f(x,y)} - h_{p(x,y)}}{dt_a}, \qquad (10)$$

where $\boldsymbol{V_z}$ is the vertical mesh velocity, h_f the nodal height of the current surface, h_p the height of the previous surface, and dt_a the ASPECT timestep.

Because FastScape represents a 2D surface in X and Y and the ASPECT model is a 2D slice in X and Z, vertical mesh velocities computed from the FastScape are averaged along Y. ASPECT then computes the internal changes of the mesh by solving the Laplace equation constrained by the surface mesh velocities (Rose et al., 2017). ASPECT subsequently responds to the topography changes during the solving of Eqs. (1-4) and the process repeats in the next timestep.

However, in subsequent timesteps only the surface velocities are sent to FastScape, while FastScape retains its own copy of the surface topography. This is done to avoid resolution loss in the topography.

In 2D models, FastScape is geometrically initialized with an extent in the Y-direction that is chosen by the user (here 100 km), and an X-length that is the ASPECT length plus two additional FastScape nodes on either side. These additional nodes represent FastScape "ghost nodes" that exist outside the ASPECT model domain, and thus the values are not considered when interpolating the surface back to ASPECT. The ghost nodes are primarily used to avoid boundary artifacts in FastScape (i.e., no uplift from advected topography) from appearing in ASPECT. To avoid issues that may arise from artificial boundary slopes, the ghost nodes are updated each timestep to be identical to the nearest ASPECT boundary node.

2.4 Fault extraction and analysis

To perform a comprehensive fault analysis, we extract fault networks from our model results using tools from the field of computer vision (https://github.com/thilowrona/fatbox). This process describes fault systems as 2D networks (or graphs, i.e., structures consisting of nodes and edges), where faults are sets of connected nodes. The fault extraction workflow consists of five main steps: 1) Thresholding: We separate shear zones from the background of our model using a plastic strain threshold of 10% of the maximum non-initial plastic strain, or anything above 1 (fully weakened). This value assures the extraction of all major shear zones from our models. 2) Skeletonization: We collapse these shear zones to one-pixel wide lines that represent discrete faults using skeletonization (Guo and Hall, 1992). 3) Connecting components: we label adjacent pixels as connected components (Wu et al., 2009). 4) Graph building: We build our graph from these components using pixels as nodes and connections as edges. 5) Junction splitting: We split up triple junctions to identify individual fault and remove any faults less than 1.5 km in length.

Once fault networks are extracted from each timestep, we correlate them across timesteps to track their temporal evolution throughout the simulation. This correlation relates faults through time based on their geometric similarity, allowing for faults to initiate, merge, split and die.

Once correlated, we can track fault and fault system properties through time. For our analysis, we focus on the number of faults, fault lengths (sum of edges) and fault displacements. Fault displacement is computed as the cumulative sum of an individual fault's slip from all previous timesteps, and the fault slip is computed from the velocity difference between hanging wall and footwall across the fault. Because of this, displacement held on a fault is sensitive to how long a fault is active for.

2.5 Model setup

To investigate fault system evolution in response to erosion and sedimentation during asymmetric, symmetric, and wide rifting, we set up a rectangular 2D tectonic ASPECT model with dimensions 450x200 km (X and Z) initialized with 4 rheologic layers (Fig. 1): a wet quartzite upper crust (20 km thick; Rutter and Brodie, 2004), wet anorthite lower crust (15 km thick; Rybacki et al., 2006), and dry olivine mantle lithosphere extending to the Lithosphere-Asthenosphere Boundary (LAB) that is set to a value typical of a non-orogenic or cratonic intracontinental setting (120 km; Artemieva, 2006; Pasyanos et al., 2014). Beneath the LAB, asthenospheric material is composed of wet olivine (Hirth and Kohlstedt, 2003). To initiate continental rifting in the model center, we thicken the warmer upper crust to 25 km (leading to a total crustal thickness of 40 km) and thin the mantle lithosphere so that the LAB still occurs at

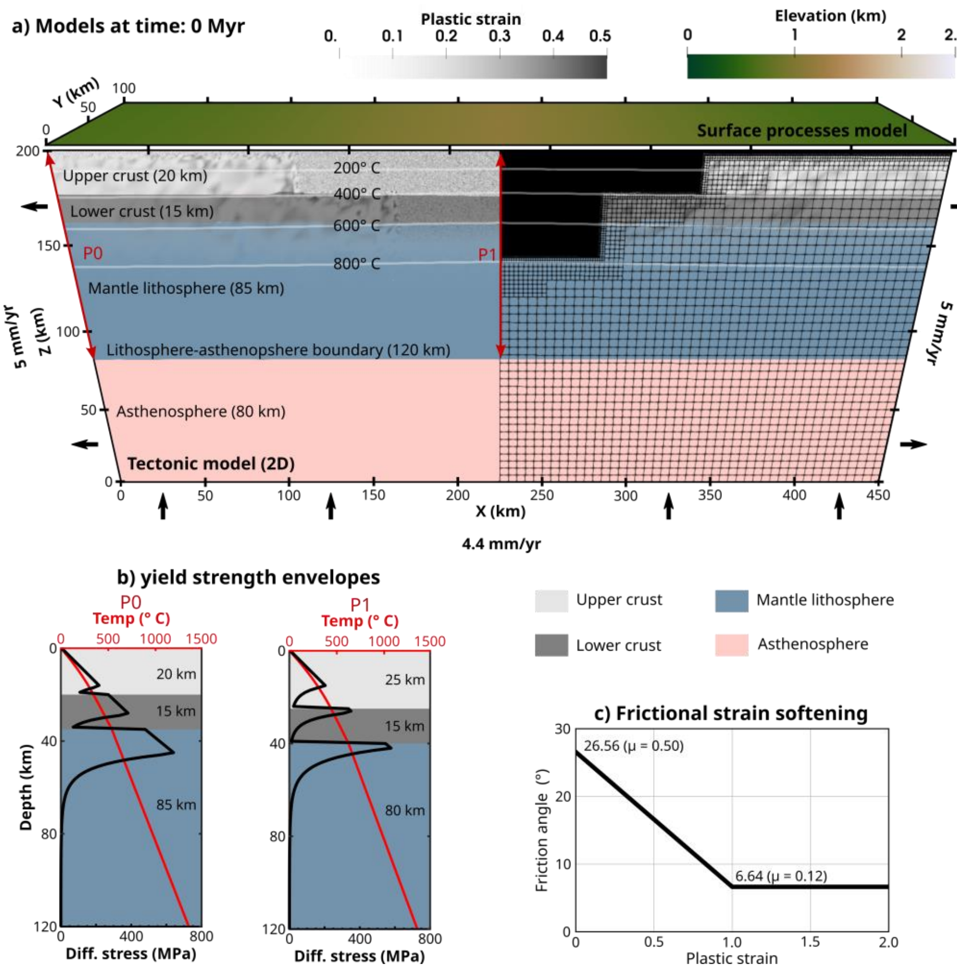

Figure 1. Reference asymmetric rift model setup at 0 Myr. a) Topography of the surface process model (FastScape) is shown on top colored by elevation. Below is the 2D tectonic model ASPECT colored by material layers. White lines indicate temperature contours. Red lines show strength profile locations for the outer (P0) and central (P1) portions of the models that have different layer thicknesses. Right side shows the model mesh refinement. b) Yield strength profiles P0 and P1 indicated in A, showing the integrated strength (black) and temperature (red). c) Graph showing the plastic weakening interval.

120 km. In addition, we distribute randomized initial plastic strain within the model domain mimicking small-scale inheritance. In all models, the value of the compositional fields is prescribed along the top and bottom boundaries. Any increases in surface topography from FastScape due to sediment deposition and not tectonics will thus be considered as sediment accumulation.

The model initial temperature is prescribed using a steady-state geotherm from the surface to the LAB at 120 km. Below the LAB, temperature is determined by a mantle adiabat. Temperature boundary conditions fix the top boundary at 0° C, the bottom temperature is prescribed according to the initial mantle adiabat, and the left and right boundary are prescribed with a zero heat-flux.

The left and right boundaries are extended at a rate of 5 mm/yr, giving a total extension rate of 10 mm/yr, which amounts to 300 km of total extension over 30 Myr. Outflow at these boundaries is compensated by inflow along the bottom boundary (~4.4 mm/yr) to conserve volume. The top boundary is deformed using FastScape.

On timestep 1 FastScape is initialized as a 2D surface that matches the initial ASPECT surface (including initial topography) where the user-defined ASPECT Z-extent is an elevation of zero in FastScape. To simulate erosion and deposition, we utilize the marine and land components of FastScape and assume a sea-level 500 m below the initial ASPECT height. Above sea-level, we use a diffusion coefficienct of $5 \cdot 10^{-3}$ m^2/yr for bedrock and sediment (Martin, 2000; Densmore et al., 2007; Armitage et al., 2013). Since the bedrock erodibility represents multiple factors such as precipitation, lithology, and vegetation (Whipple and Tucker, 1999) and can vary over multiple orders of magnitude in nature (10^{-7} to 10^{-2} $m^{0.2}$/yr; Stock and Montgomery, 1999), we vary K_f between 10^{-6} and 10^{-4} $m^{0.2}$/yr to represent low to high surface process efficiency (Wolf et al., 2021). Below sea-level, we use a diffusion coefficient consistent with marine settings (200 m^2/yr; Rouby et al., 2013). Additionally, in the marine environment we assume there is some pelagic/hemipelagic sedimentation and add a uniform time-dependent topography increase to regions below sea-level accordingly (Table S2).

The model mesh resolution ranges from a minimum 10 km to a maximum of 156 m in the sediment composition. Areas without sediment can reach a maximum resolution of 312 m, which occurs in any cell that contains particles. Passive particles are initially uniformly distributed within a 100 km wide box in the upper 55 km of the model around the center (Gassmöller et al., 2018). The mesh is updated every 5 timesteps, and as the particles are advected with the material velocity the faulted areas remain highly refined. The FastScape mesh has a uniform resolution of 312 m.

Our models provide a detailed look at fault and landscape evolution in 2D rift systems, however, multiple limitations exist. While extensional slip along our faults accounts for most of the expected extension in the model (according to the fault analysis results; Fig. S1), we do not include faults smaller than 1.5 km in the analysis and thus neglect smaller fault dynamics, especially in late breakup stages where the brittle envelope may be thinner than 1.5 km. Additionally, since our tectonic model is 2D, we do not consider how fault system evolution is impacted along-strike by variability in loading related to erosion, deposition and inheritance (e.g., Heron et al., 2019; Naliboff et al., 2020). Also, we assume our models represent passive margins without magmatic activity, as such we do not account for the inclusion of smelt possibly altering rift dynamics (e.g., Bahadori and Holt, 2019).

3 Results

We present the general and fault system evolution of three different model setups that result in endmembers for rifted margin formation: narrow rifting leading to (1) asymmetric and (2) symmetric margin configurations and (3) rifting where deformation occurs over a wide region resulting in a large zone of thinned continental crust. Our reference model of an asymmetric narrow rift has been described in the previous section. To achieve a symmetric narrow rift, we reduce the frictional angle weakening from the 75% used in the reference model to 50% (Huismans and Beaumont, 2003). Wide rifts generally occur in regions with thick crust and high heat flow (Buck et al., 1999), as such we again use a frictional angle weakening of 50% and increase the radiogenic heating of the upper crust from $1.0 \cdot 10^{-5}$ to $1.5 \cdot 10^{-5}$ W/m^3 and change the crustal thicknesses to 35 km upper crust and 5 km lower crust in the middle of the model domain, and to 25 km of upper crust and 10 km lower crust elsewhere. All other parameters remain identical between the three model sets.

3.1 Asymmetric rift systems

In this section we discuss the reference asymmetric model (bedrock erodibility, $K_f = 10^{-5}$ m$^{0.2}$/yr) and compare it to additional models where we have no Surface Processes (SP) or vary the K_f value. We find from a quantitative analysis of the evolution of the number and cumulative length and displacement of active faults in the system, that regardless of the SP efficiency the system can be divided into five distinct phases: 1) *distributed deformation and coalescence*, 2) *fault system growth*, 3) *fault system decline and basinward localization*, 4) *rift migration*, and 5) *continental breakup*.

3.1.1 Asymmetric reference model evolution

Initially, many small faults accumulate small amounts of strain within the model center. By 0.4 Myr (Fig 2a; Video S1), these faults have coalesced into two major normal faults that connect at ~45 km depth in the mantle lithosphere (Huismans and Beaumont, 2003; Albaric et al., 2009). These major faults accumulate displacement, forming rift flanks as the central block sinks. This sinking causes the major faults to define the land and sea boundary, and the region between them becomes a sediment trap. As the uplifted rift flanks erode, a seaward thinning basin forms between the border faults (Pérez-Gussinyé et al., 2020). At ~3 Myr, the left-dipping border fault links to the viscously deforming mantle lithosphere through a secondary left-dipping fault in the lower crust of the central block. The linkage of these faults generates a concave downward left-dipping detachment fault (Fig. 2b; Lavier and Manatschal, 2006). Necking uplifts and rotates the detachment fault to lower angles and provides a weak base for new faults to form and dismember the central block (Huismans and Beaumont, 2003). Subsequently, the initial basin is split and separated by exposed upper crust (Fig. 2c). By ~7 Myr, the two major border faults become inactive as the detachment fault connects to the younger, smaller faults forming in the center of the model, creating an asymmetric rift.

At ~7 Myr, the rift system migrates to the left (Brune et al., 2014). Large faults that connect from the surface to the detachment fault dissect and rotate the crust to the right of the rift, creating additional basins between the blocks (Fig. 2f). At ~11 Myr, there is a rightward shift in the rift as

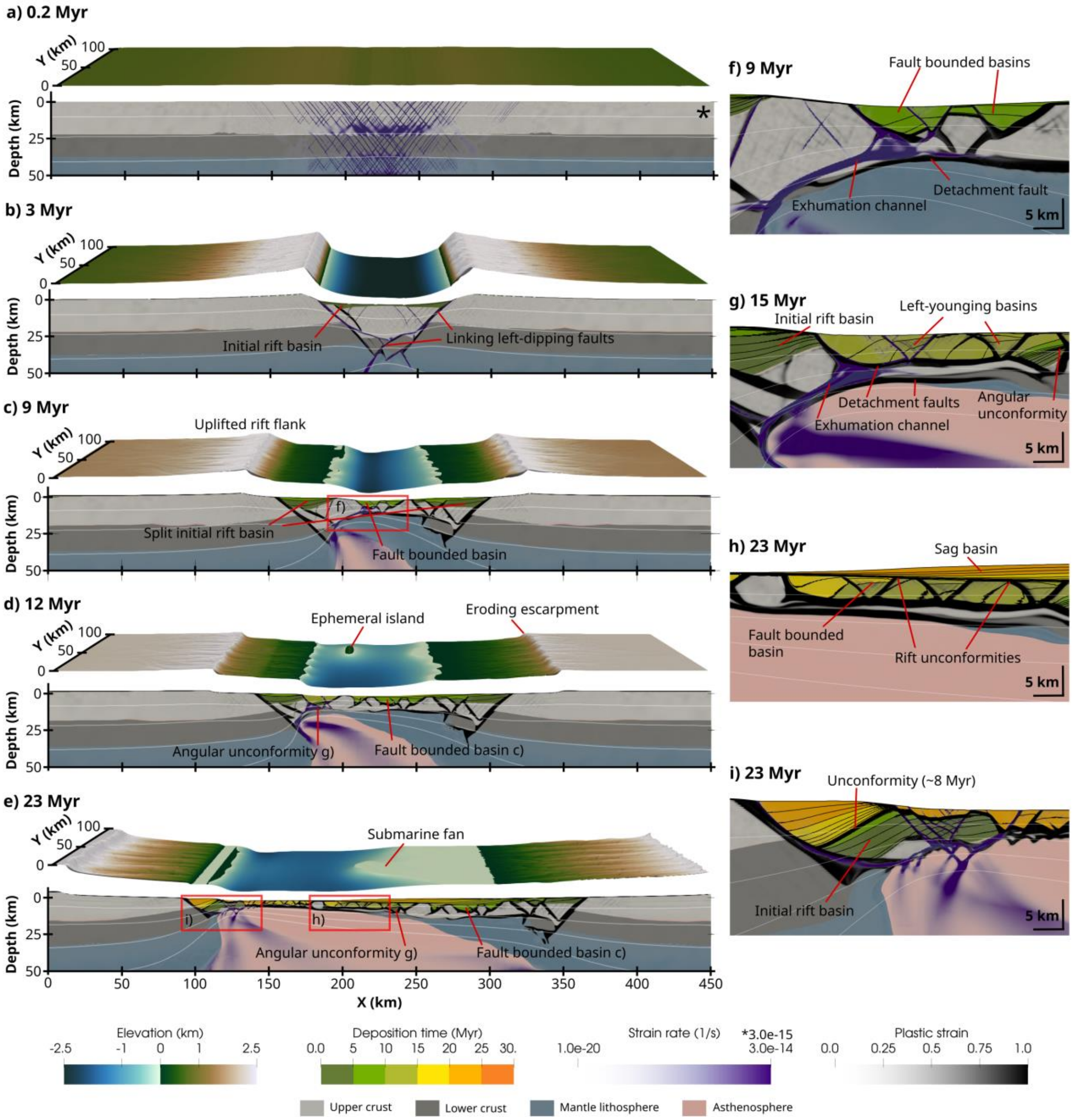

Figure 2. Evolution of the reference asymmetric rift model (Videos S1 and S2) depicting the formation of surface faults within a thinning brittle layer, and underlying detachment faults related to an exhumation channel. (a-e) The FastScape model (3x vertical exaggeration) is shown on top. The ASPECT model is shown on the bottom showing the strain rate (transparent to purple), plastic strain (transparent to black), isotherms, and sediment deposition time (shown in 5 Myr intervals). White contours indicate temperature between 200 and 800 C. *Strain rate scale is reduced in A to highlight distributed deformation. (f-i) Close up views to highlight specific basin and fault features, with black contours indicating sediment age at 1 Myr intervals.

the initial detachment fault becomes inactive, and a second detachment fault forms and connects to the initial left border fault that resumes activity. To the right of the rift, the crust is thin by 12 Myr (~4 km) and faulting primarily occurs within the sedimentary infill (Fig. 2c). As the rift migrates, conjugate faults form in succession, with fault-bounded left-younging basins being deposited adjacent to the left half of the initial rift basin (Fig. 2g). Around this time, rotation of an upper crustal block leads to emergence of basement above sea-level creating an ephemeral island (Chenin et al., 2019). As migration continues, the older inactive fault-bounded basins are overlain by sediment marking multiple rift migration unconformities (Fig. 2h; Pérez-Gussinyé et al., 2020). Eventually, slip on the initial left border fault that bounded the initial rift basin increases, tilting the sedimentary layers and causes deposition of new sediment on top of the old rift basin (Fig 2i). Because of this tilting, the oldest sediment is exposed near the migrating rift, and parts of the initial rift basin are translated to the right side of the rift. At ~23 Myr, there is an ~10 km rightward shift in deformation as migration ceases and seafloor spreading begins (Fig. 2d), this shift in deformation causes fault-block emersion of the marine shelf. Subsequently, there is a short phase of stability (~23-25 Myr) before asymmetric sea floor spreading initiates and migrates to the right.

3.1.2 Asymmetric fault system evolution

We use our fault extraction toolbox (Fatbox) to examine the quantitative evolution of the rift's fault network in terms of the number, cumulative length, and displacement held on active faults in the system. Using the plastic strain, we can track the entire fault system, however of particular interest are the active faults. To this end, we consider any fault with a maximum slip rate >0.1 mm/yr as active, a value on the lower end of fault slips seen in the Great Basin (0.06 to 3 mm/yr; Depolo and Anderson, 2000). If the slip along an individual fault falls below this value, it no longer contributes to the cumulative total in length and displacement. Using this value, the active faults account for 97.8% of the total slip held on the tracked faults (Fig. S2), illustrating the robustness of our approach.

The active faults in the system suggest that the model evolves according to five separate phases (Fig. 3, Video S2):

Phase 1: Distributed deformation and coalescence (~0-1 Myr). During this phase many small faults form and compete. The phase has a large total fault system length and number of faults that quickly declines as deformation localizes on a few major faults.

Phase 2: Fault system growth (~1-7 Myr). The faults formed during phase 1 coalesce into two major border faults, marked by a reduction in the fault number and length. As extension continues, new, smaller faults form between the initial ones leading to a growth in the number, length, and displacement of the active faults. Over time slip on the inner faults increases relative to that on the border faults, until eventually the border faults become largely inactive as deformation localizes basinward.

Phase 3: Fault system decline and basinward localization (~7-11 Myr). We distinguish the start of phase 3 by one of the border faults becoming inactive. As the outer faults, particularly those opposite the direction of rift migration, become inactive, the fault system shows a decrease in the number, length, and displacement held on the active faults. Since the brittle layer thins, new

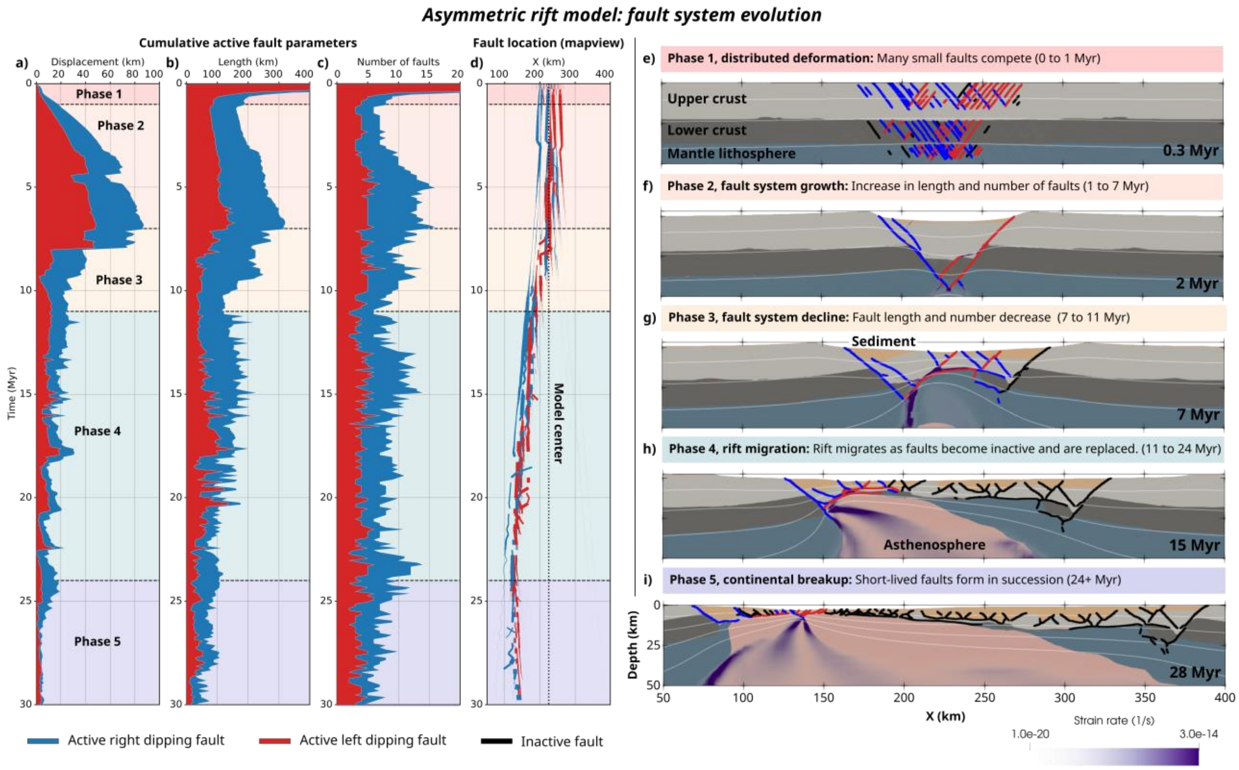

Figure 3. Active fault network evolution of the asymmetric rift reference model showing the five fault system deformation phases that relate to structural domains. (a-d) Graphs depict the change in cumulative active fault properties and fault location through time. Blue indicates right dipping faults and red left dipping faults. The background is colored by the deformation phases. (e-i) Snapshots of the ASPECT model during different phases. The extracted fault network is overlain on the model in black (inactive fault), blue (active right dipping fault), and red (active left dipping fault).

faults are shorter than previous ones. Also, because older faults become inactive at this time there is a net loss in the total displacement held on the active faults.

Phase 4: Rift migration (~11-24 Myr). During rift migration, faults are shorter lived compared to the previous phases, with new faults frequently forming and replacing older faults (~1-2 Myr activity time). This shorter activity time leads to less displacement on active faults relative to phases 2 and 3. While there is some variation in the fault number and length of the system, generally this phase shows a gradual decline in, most notably, the cumulative length of the system as the brittle layer the faults form in continues to thin before breakup.

Phase 5: Continental breakup (~24 Myr to model end). We determine the breakup phase to have started when the rift jumps seaward and completes the separation of continental lithosphere. While the number of faults remains similar to phase 4, the cumulative length of the system continues to decrease as the sediment layer thins, and there is a noticeable drop in the displacement. The drop in displacement likely relates to the lifespan of faults, when faults are replaced more quickly there is less time to accumulate displacement before they become inactive.

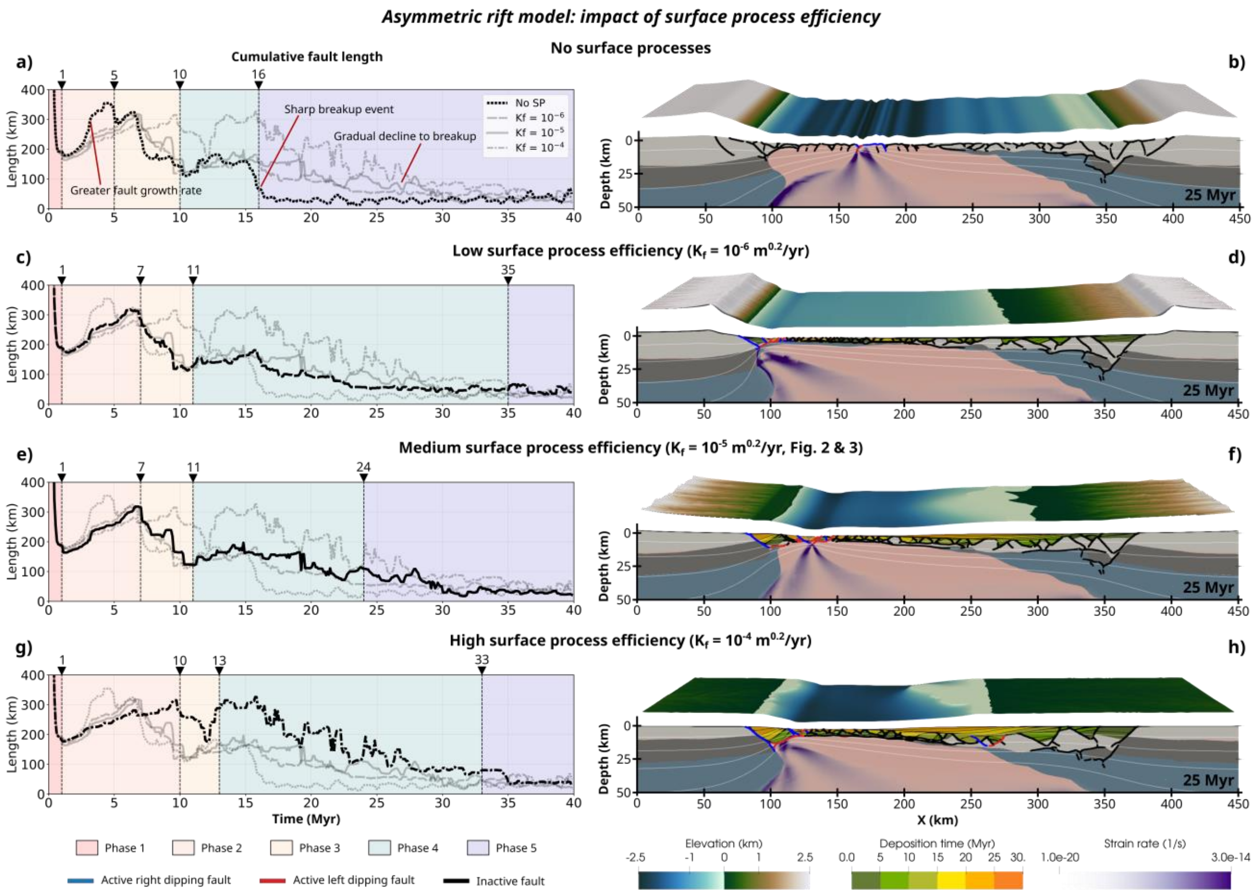

Figure 4. Comparison of the active fault network's cumulative length between asymmetric rift models with varying surface process efficiency, displaying the greater periods of fault system growth and rift migration with surface processes. a) Fault length graph for the model without surface processes, where the background is colored by the phase. The dark black line represents the current no surface processes model while the semi-transparent lines indicate the other models. b) Snapshot of the model without surface processes at 25 Myr. The extracted fault network is overlain on the model in black (inactive fault), blue (active right dipping fault), and red (active left dipping fault). Low (c-d), medium (e-f), and high (g-h) surface process efficiency models.

3.1.2 Effects of surface process efficiency on Asymmetric rift systems

To discuss how SP efficiency affects the phases of fault system evolution (Fig. 4), we focus on the cumulative fault length as it best distinguishes the phases. Phase 1 is similar regardless of SP and the value of bedrock erodibility. In phase 2, faults grow slower with greater SP efficiency, and the shift into fault decline (phase 3) is delayed. Phase 3 is similar in all the models, though more faults are active at a given time in the model with high SP efficiency, making it harder to distinguish the shift from phase 3 to 4 (Fig. 4g). Breakup (phase 5) is clearly visible in the model without SP, wherein the length of the active fault system sharply decreases at breakup (Fig. 4a). In models with SP, the cumulative length gradually declines during migration as the sediment layer thins leading to a less noticeable breakup event. Additionally, the sediment layer delays breakup, although the amount of sediment does not appear to influence how much breakup is delayed (i.e., breakup occurs at 16 Myr with no SP, 35 Myr with low SP efficiency, 24 Myr with medium efficiency, and 33 Myr with high efficiency; Table S3).

3.2 Symmetric rift system

In the same manner as the previous section, here we cover the evolution of a symmetric narrow rift. We find that the symmetric setup evolves according to 4 distinct phases similar to what is seen in the previous model, but without rift migration (phase 4).

3.2.1 Symmetric reference model evolution

The model starts with many faults accumulating small amounts of strain (Video S3), which by ~1 Myr have coalesced onto two major ~50° dipping conjugate faults (Huismans and Beaumont, 2003). These major faults define the land-sea boundary, and the region between is filled with sediment forming an oceanward thinning rift basin by ~4 Myr. During the necking process, rotation of the initial major faults generates many parallel-seaward-dipping faults that breakup the central block (Nagel and Buck, 2004). This breakup results in a relatively symmetric splitting of the initial rift basin, with new faults forming between the basins and a similar inward shift of the land-sea boundary. By ~8.5 Myr, the deeper portions of the initial major faults have rotated to ~35° and become inactive. Necking continues as the remainder of the central block is broken up. New basins form in the model center as the rift flanks and the, now exposed, initial rift basin halves are eroded and deposited. At ~14 Myr seafloor spreading starts.

Initially, the nearby uplifted margins provide a large sediment flux and seafloor spreading is sediment-dominated. Primarily, seaward dipping faults form successively within the sediment creating multiple fault-bounded basins. Simultaneously, short migration events generate landward dipping faults that extend from the sediment basement into the asthenosphere, though the cumulative asymmetry of these events produces an overall symmetric system (Huismans and Beaumont, 2003). As the uplifted margins move further from the active rift zone, less sediment reaches the model center and progressively smaller faults form within the thinning sediment layer. Near the margins, sediment is deposited on top of the inactive faults marking multiple rift unconformities with the fault-bounded basins. By ~25 Myr very little sediment reaches the model center and basin formation halts as seafloor spreading becomes sediment-starved.

3.2.2 Symmetric fault system evolution

Using the same phase definitions as described in Section 3.1.2, we find that the fault system in the symmetric rift model evolves according to 4 phases (Fig. 5, video S4).

Phase 1: Distributed deformation and coalescence (~0-1.5 Myr). Many faults compete before coalescing. In the fault system, this appears as a high number of faults and cumulative fault length that rapidly declines.

Phase 2: Fault system growth (~1-8 Myr). The major border faults remain active while new faults form and dismember the central block. This is seen as a period of increase in fault system length, number, and displacement.

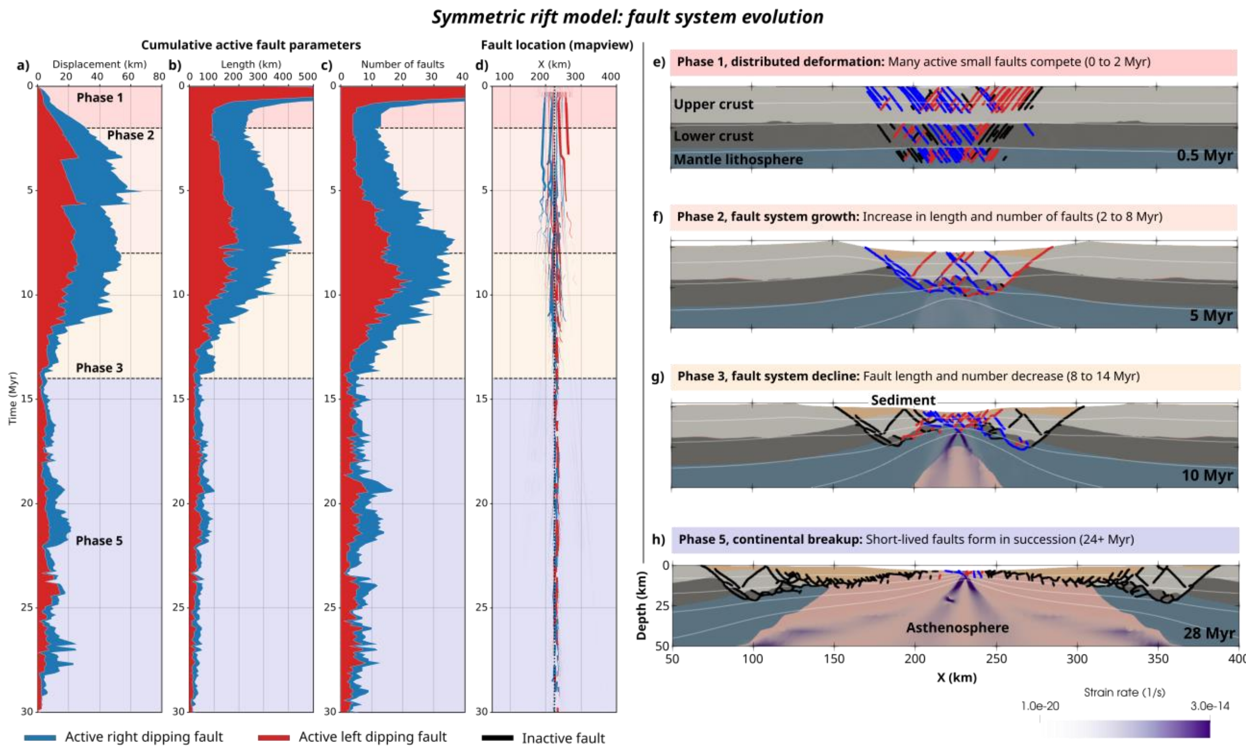

Figure 5. Active fault network evolution of the symmetric rift reference model, showcasing the basinward migration of deformation through the phases. Refer to figure 3 for explanation.

Phase 3: Fault system decline and basinward localization (~8-14 Myr). By 8 Myr, the border faults become inactive as deformation localizes in the central region. This leads to a decrease in the number of faults and the cumulative length of the system.

Phase 4: Rift migration. This phase is not expressed in this setting.

Phase 5: Continental breakup (~24 Myr to model end). In this phase, short faults form in succession in the thin sediment layer. Because faults are smaller and shorter-lived in this phase, the fault system shows a lower number of faults, fault length, and displacement compared to the previous phases.

3.2.3 Effects of surface process efficiency on Symmetric rift systems

Similar to section 3.1.3, we run four models with varying SP efficiency (Fig. 6). Phase 1 is consistent regardless of SP. Phase 2 lasts longer with increasing SP efficiency (~2 Myr difference with no SP vs. high efficiency). Additionally, less effective SP leads to more faults and a greater cumulative length. SP does not generally affect phase 3, with the exception of the high efficiency case where it lasts significantly longer. In all other models, phase 5 (breakup) is delayed proportional to SP efficiency. In the high SP efficiency case, there is a gradual decline in the fault system length and continental breakup is not clearly distinguishable in this variable.

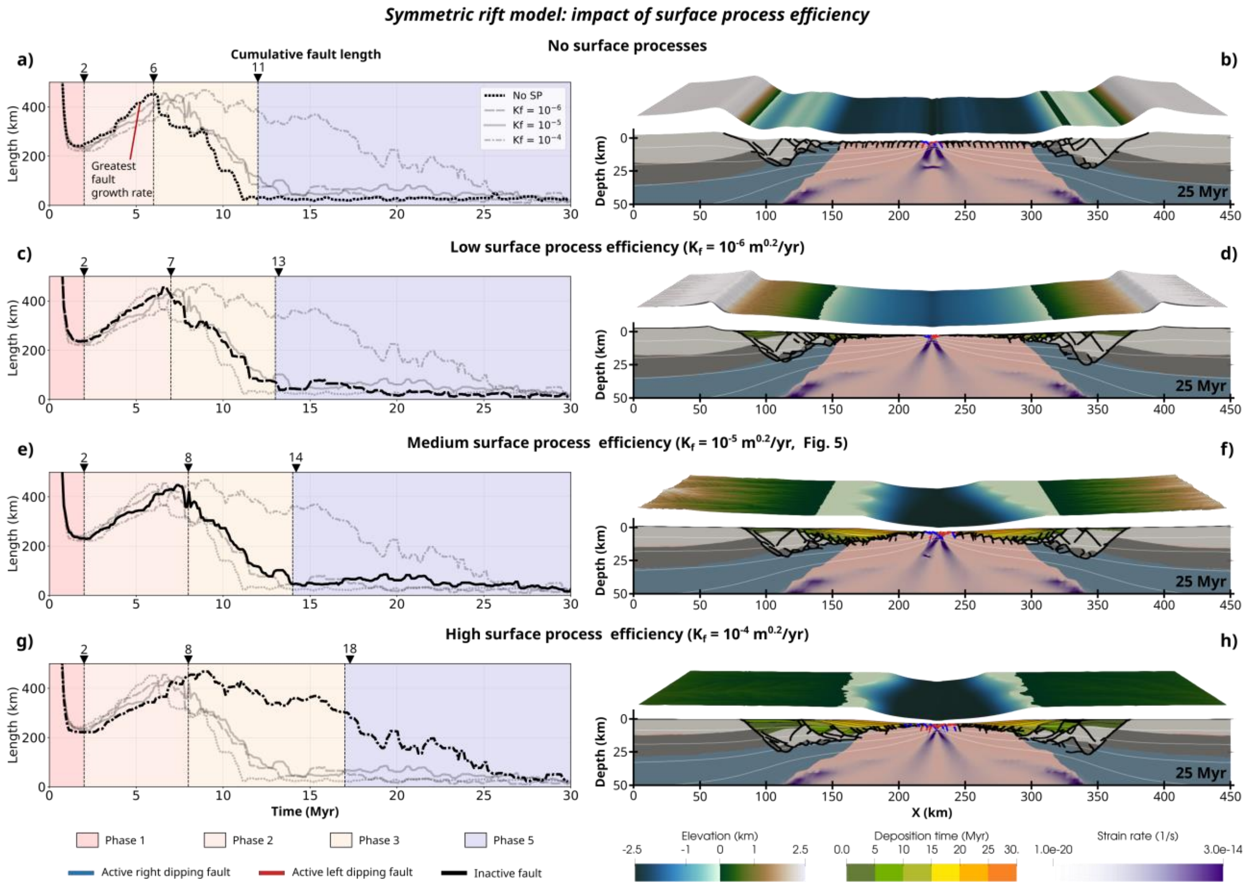

Figure 6. Comparison of the active fault network's cumulative length between symmetric rift models with varying surface process efficiency, depicting the delay in breakup with greater surface process efficiency. Refer to figure 4 for explanation.

3.3 Wide rift system

Here we examine the evolution of a wide rift model with varied SP efficiency and find that the fault system evolves in four phases similar to the narrow symmetric model, although the timing of phases differs.

3.3.1 Wide reference model evolution

During the distributed deformation phase, many faults form within the brittle portion of the upper crust (Video S5). By ~1 Myr, these have localized on two sets of conjugate faults and one right-dipping fault ~50 km left of the model center. As the faults accumulate displacement, each becomes associated with a basin and a shallow sea or lake. During the necking process fault rotation to lower angles widens basins and faults form over a wider region. Generally, new faults dip towards the rift center forming half-graben basins (Leeder and Gawthorpe, 1987) whose strata dip away from the rift center. By 12 Myr, multiple faults have formed over a region spanning ~260 km and the multiple seas associated with each fault have merged into a single sea. At this time many small basins exist and are separated by exposed upper crustal blocks. While the outer basins dip away from the rift center, near the rift center tilting is more varied.

Progressively smaller faults and basins form as necking continues and the remaining upper crust is thinned. By ~25 Myr, deformation has localized in the center where the upper crust is entirely gone, and sediment-dominated continental breakup occurs. At this time the previously-active distal faults have been overlain with sediment marking multiple rift unconformities. From here until the end of the model the rift migrates to the right driven by the thin layer of sediment overlying the rift.

3.3.2 Wide fault system evolution

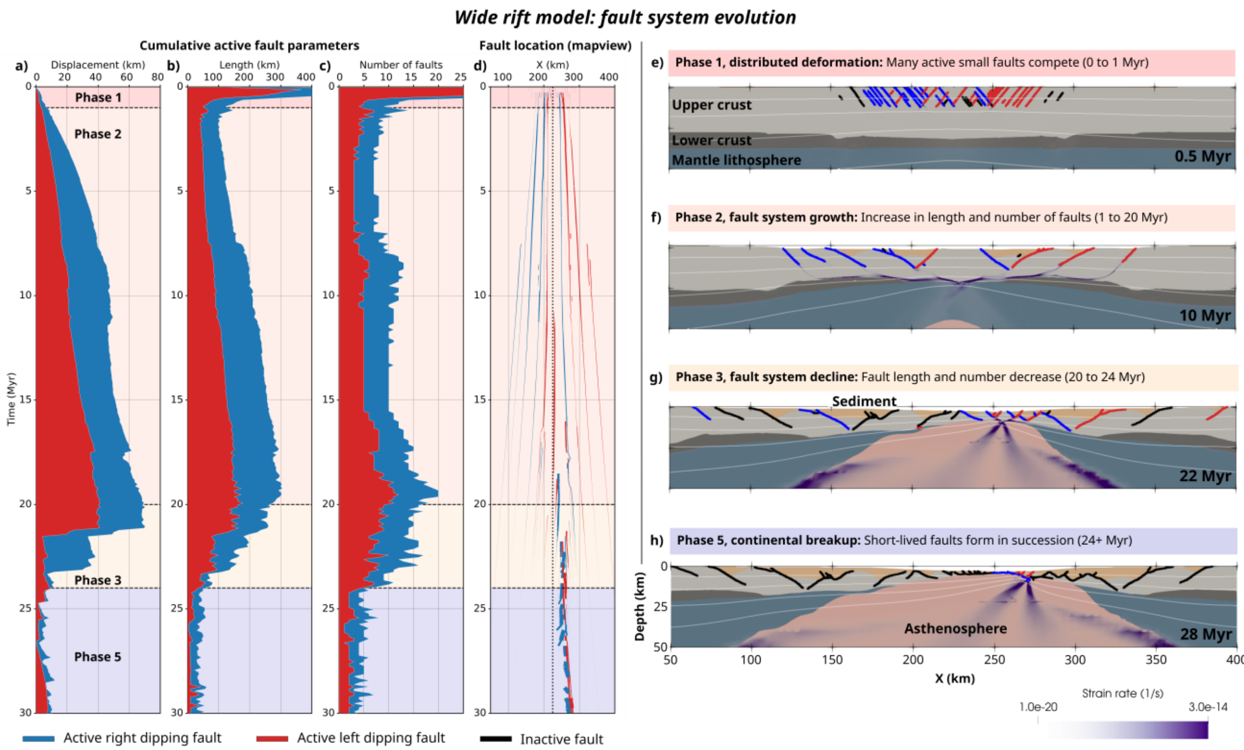

Figure 7. Active fault network evolution of the wide rift reference model, showcasing the greatly extended fault growth phase relative to asymmetric and symmetric models. Refer to figure 3 for explanation.

We evaluate the evolution of the fault system in the wide rift (Fig. 7, video S6) using the previously defined phases:

Phase 1: Distributed deformation and coalescence (~0-1.5 Myr) where many faults compete and coalesce.

Phase 2: Fault system growth (~1.5-20 Myr). New faults form while the initial ones remain active. As faults form at a slower rate and are active much longer in this model than in the asymmetric or symmetric cases, this phase is greatly extended.

Phase 3: Fault system decline and basinward localization (~20-24 Myr). When only upper crust remains in the rift center deformation localizes in the region. This shift in deformation deactivates the long-lived faults leading to a drop in fault number, length, and displacement.

Unlike the previous cases, fault cessation does not necessarily start with the outer faults and move inward.

Phase 4: Rift migration. This phase is not expressed in this setting.

Phase 5: Continental breakup (~24 Myr to model end). By ~24 Myr, the upper crust is separated, denoting continental breakup. In this phase, short seaward dipping faults form sequentially while the rift migrates. This phase shows much lower fault number, length, and displacement than phases 1-3, and the properties remain relatively constant.

3.3.3 Effects of surface process efficiency on Wide rift systems

By varying the efficiency of SP, we find that phase 1 is similar in all cases, except that there is a trend that higher efficiency leads to localization on a fewer number of faults (Figs. S3 and S4) and, thus, to a lower cumulative length of faults (Fig. 8). Like previous asymmetric and symmetric cases, SP extend the fault growth (phase 2) phase. While the initial inclusion of SP causes a large delay in the start of phase 3 (15 Myr without SP vs. 20 Myr with low SP efficiency), the difference between low and medium SP efficiency is negligible. However, high SP efficiency shows another large delay to the start of phase 3 (20 Myr at medium SP efficiency vs. 23 Myr at high efficiency). Additionally, in phase 2 cumulative length in the model without SP increases at a greater rate than those with SP until ~300 km. Subsequently both fault number and length remain relatively constant until phase 3. Interestingly, phase 3 in the low and medium SP efficiency models also starts when the cumulative length reaches ~300 km, although in the high efficiency model phase 3 is delayed until the system is ~350 km in length. Phase 3 is similar regardless of SP, with all models declining in cumulative fault length over ~3-5 Myr until continental breakup (phase 5). Unlike the asymmetric and symmetric cases, breakup is clearly represented in fault system length, regardless of SP efficiency.

4 Discussion

4.1 Effects of surface process efficiency on rifting

While each of the three rift types exhibits different fault structures and phase timings, surface processes (SP) had a similar effect on the models regardless of the rift type. In particular we find that SP efficiency affects the longevity of individual faults, the structure of fault systems, and the timing of rift phases. This agrees with previous studies indicating that faults localize faster and remain active for longer when sediments load the hanging wall and erosion releases the footwall (Maniatis et al., 2009; Andrés-Martínez et al., 2019; Theunissen and Huismans, 2019). As a consequence of prolonged fault activity, there is less incentive to create new faults as a greater portion of the prescribed system slip is held on the older faults. This explains why for less effective SP, a greater number of faults form during phase 2 (fault system growth) and phase 3 (fault system decline and basinward localization). This can be seen when comparing the cumulative length of active faults, where during phase 2 the cumulative length increases faster in models with less SP efficiency (e.g., Fig 4). The greater rate of increase in cumulative length during the early phases results in more shorter faults during the early phases for rifts with less SP efficiency (Figs. S3, S4, S5, S6) and predicts that in sediment-starved margins the architecture during early rifting is more complex with a greater number of interconnected faults.

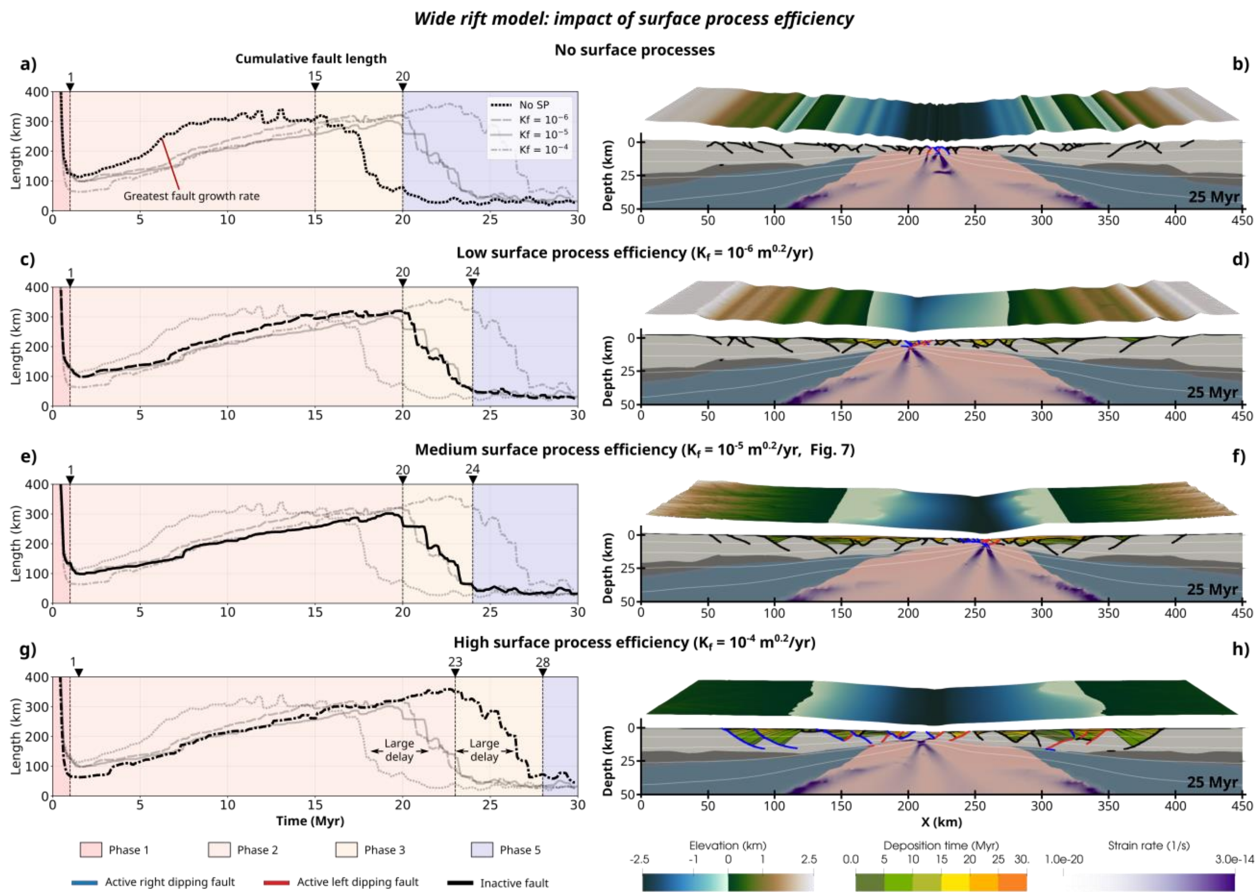

Figure 8. Comparison of the active fault network's cumulative length between wide rift models with varying surface process efficiency, demonstrating the greater fault growth rate and fault structure complexity in models without surface processes. Refer to figure 4 for explanation.

While the general structural evolution of rifting in terms of symmetry and rift width is largely independent of erosion and sedimentation, our results show that individual rift phases are prolonged when surface processes are accounted for (cf. Buiter et al., 2008; Choi et al., 2013; Olive et al., 2014). Specifically, fault system growth (phase 2) lasts 1 to 8 Myr longer depending on the rift type and amount of erosion and sedimentation, whereas rift migration (phase 4) lasts 6 to 20 Myr longer with the addition of surface processes (Fig. 4). Hence, rifted margins with thick syn-rift sediment sequences require a larger amount of extension to achieve continental breakup (Clerc et al., 2018) and are more prone to the occurrence of rift migration (Buiter, 2021). This also suggests that along-strike changes in sediment supply could lead to neighboring portions of a rift system evolving at different paces, with sediment-starved rift segments reaching breakup and ocean formation sooner than sediment-rich segments.

4.2 Rift migration, detachment faults and serpentinization

In our models rift migration is facilitated through a combination of an exhumation channel (Brune et al., 2014) and slip along detachment faults (Fig. 9). Material in the exhumation channel zone

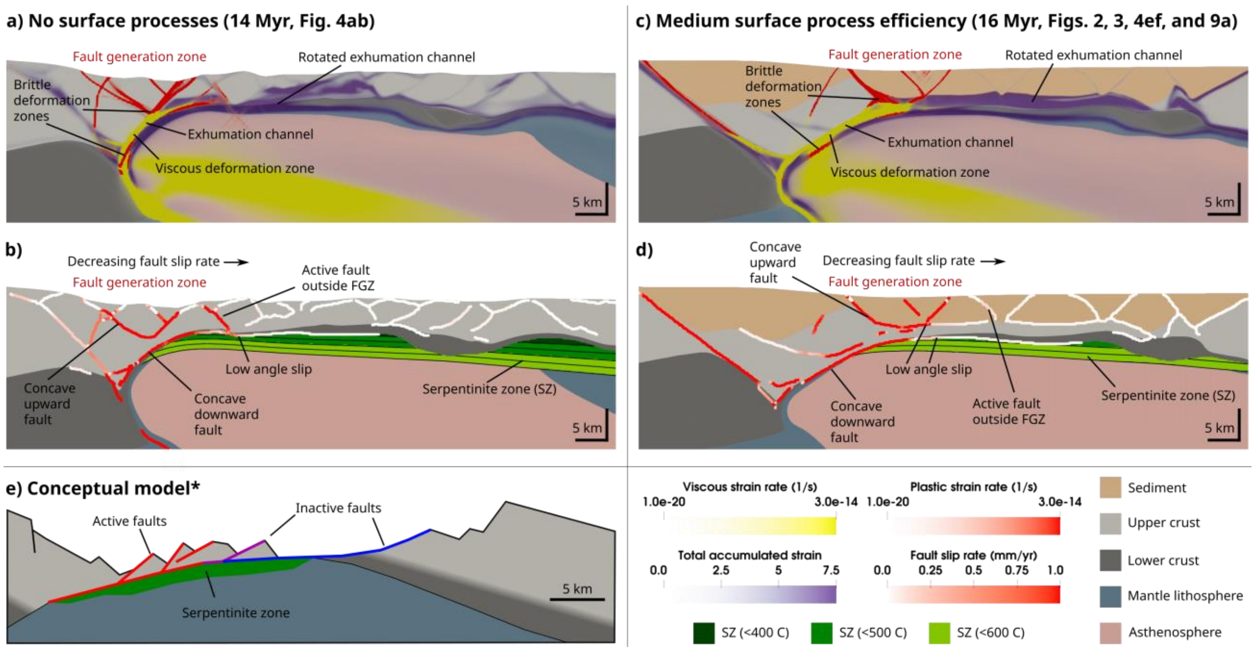

Figure 9. Rift migration processes, showing the brittle and viscous deformation inside the exhumation channel, and low angle slip along detachment faults relative to regions where serpentinization would be possible. a) Snapshots of the no surface processes model that showing the plastic strain rate (opaque-red), viscous strain rate (opaque-yellow), and total accumulated strain (opaque-purple). b) Identical to a) showing the fault slip rate (white-red) along the extracted fault network. Regions within temperature conditions for serpentinization are colored at 100° C intervals, with black contours denoting 50° C intervals. c) Snapshots of the medium surface process efficiency reference model like in a). d) Snapshots of the medium surface process efficiency reference model like in b). e) Modified conceptual model from Lymer et al., 2019, showing the region of serpentinization. Red indicates active faults, and purple and blue inactive faults.

undergoes large amounts of brittle and ductile deformation. At the base of the zone, a tongue of plastically yielding lower crust generates a concave downward detachment fault. Continued extension rotates the fault and adjacent ductile shear zone to sub-horizontal angles, creating a weakened channel of material. The geometry, location and kinematic history of this channel reproduces the characteristics of the prominent "S reflector" at the West Iberian margin (Hoffmann and Reston, 1992; Reston et al., 2007). A secondary concave upward detachment fault forms at the surface and connects to the concave downward fault in the weakened channel. Rooted in the second detachment fault along the weakened channel, a zone of high plastic strain generates sequential conjugate or seaward dipping normal faults.

Our models suggest that detachment faults form near a frictionally and viscously weakened exhumation channel and are rotated subhorizontally. Slip along these detachment faults is greater in the portions at higher angles, but low-angle slip occurs as the rotated exhumation channel translates material from the left to right margin. Normal faults form in a migrating fault generation zone that is rooted in a detachment fault. These normal faults are not exclusively active sequentially and often multiple faults are active simultaneously. Slip is greatest on newly formed faults and decreases with age and distance from the fault generation zone (e.g., Fig. 9d).

Low-angle slip in our models occurs along the rotated exhumation channel consisting of frictionally and viscously deformed material. It has been suggested that such low-angle slip requires weak hydrated rock such as serpentinite (Lymer et al., 2019). The upper temperature limit for serpentinization is not well constrained and falls between ~350-600 °C (Lavier and Manatschal, 2006; Emmanuel and Berkowitz, 2006; Pérez-Gussinyé et al., 2006; Bickert et al., 2020; Albers et al., 2021). While our models do not include the process of serpentinization, temperatures found near the detachment faults enable the generation of serpentinite in the region (Fig. 9b). This is in contrast to previous models (Brune et al., 2014, 2017) that did not have the required numerical resolution to resolve the thin mantle layer of sufficiently low temperatures. The addition of serpentinization could result in greater slip along the detachment fault, possibly increasing surface fault activity. It has also been suggested that serpentinization requires a thin, entirely brittle, crust (<10 km; Reston and Pérez-Gussinyé, 2007). We find that sedimentation increases the depth, temperatures, and the degree of viscous deformation within the rotated exhumation channel rendering it less prone to achieve serpentinization (Fig. 9cd). These factors suggest that serpentinization is more likely to occur in sediment-starved margins like the Iberian-Newfoundland margins (Whitmarsh et al., 2001; Bayrakci et al., 2016), and in the late stages of rift migration.

4.3 Rift phases and rifted margin domains

At continental rifts, crust and mantle lithosphere are successively thinned until breakup is achieved. This progressive thinning constitutes an intrinsically transient behavior of rifts, that does not occur for other plate boundary types (subduction zones, mid-oceanic ridges and strike-slip faults). This transientness is the underlying reason why rift evolution can be adequately described through distinct deformation phases (Lavier and Manatschal, 2006; Corti, 2012; Peron-Pinvidic et al., 2013; Huismans and Beaumont, 2014; Brune et al., 2017; Naliboff et al., 2017). Previous phase definitions have been based on changes in layer thickness (Lavier and Manatschal, 2006; Huismans and Beaumont, 2014; Naliboff et al., 2017) and their impact on rheology (Lavier and Manatschal, 2006; Huismans and Beaumont, 2014), or the location of faults (Corti, 2012). Here, we used a novel analysis technique to characterize rift phases in terms of active fault network properties like displacement, total fault length and fault number. In this section, we first compare the rift phases we identified in this study to previous definitions before we focus on their relevance for rifted margin domains.

Phase 1 (Distributed deformation and coalescence): Phase 1 is analogous to the early "stretching phase" (Peron-Pinvidic et al., 2013; Naliboff et al., 2017; Chenin et al., 2021). The Trondelag platform in Norway provides a remnant example of this phase (Peron-Pinvidic et al., 2013).

Phase 2 (Fault system growth): Phase 2 can be associated with the "thinning phase" (Lavier and Manatschal, 2006). It is also similar to the first phase in two-phase rifting (Agostini et al., 2009; Corti, 2012), where large faults border a central graben. Many rift segments in East Africa such as the Malawi and the Central Kenya rifts constitute examples of this phase, with active border faults surrounding the central graben (Ebinger and Scholz, 2012; Williams et al., 2019; Richter et al., 2021).

Phase 3 (Fault system decline and basinward localization): Fault system decline relates to onset of the "hyperextension phase" (Peron-Pinvidic et al., 2013) and the second phase in two-phase rifting (Agostini et al., 2009; Corti, 2012). The timing of the shift from phase 2 to 3 can vary significantly depending on the rift obliquity (Agostini et al., 2009), or as we suggest in this study, rift type (e.g., wide, symmetric, asymmetric) and the efficiency of surface processes. An active example is the northern Main Ethiopian Rift, where fault activity is localizing basinward on the Wonji fault belt (Corti, 2012).

Phase 4 (Rift migration): Rift migration is part of the “hyperextension phase” (Peron-Pinvidic et al., 2013). Through continuous activity of a migrating exhumation channel (Brune et al., 2014), it generates distinct margin asymmetry (e.g., Iberian-Newfoundland conjugates or Central South Atlantic margins, Brune et al., 2017).

Phase 5 (Breakup): Phase 5 describes continental breakup and the onset of seafloor spreading. Being the end state of continental rifting, many natural examples exist around the globe (e.g., South Atlantic, Heine et al., 2013; Red Sea, Stern and Johnson, 2019).

The five phases in this study are comparable to the deformation phases (e.g., stretching phase) linked to domains in margin architecture (Lavier and Manatschal, 2006; Peron-Pinvidic et al., 2013). Rifted margin domains comprise the 1) proximal domain (*distributed deformation and coalescence*) to the 2) necking domain (*fault system growth*), 3) hyper-extended domain (*fault system decline and basinward localization*), 4) domain of lithospheric mantle exhumation (no comparable phase), and 5) oceanic crust domain (*continental breakup*; Chenin et al., 2021). Figure 10 compares the final architecture of our medium bedrock erodibility models at 30 Myr to the structural domains, where we first define anything outside of the initial border faults as the proximal domain. Second, we examine the time when a phase ends and define any part of the margin that no longer significantly deforms after that time as part of that domain.

Our results demonstrate a close correlation between the deformation phases and the rifted margin domains (Fig. 10). Structural domains in symmetric margins, wide margins, and the margin opposite the direction of migration (right margin) in the asymmetric model progress as expected. That we see the same phase and domain progression in all models in this study regardless of the rift type (e.g., symmetric, asymmetric, or wide) and efficiency of surface processes supports the application of deformation domains to the margins of a variety of rift configurations (e.g., Chenin et al., 2021). Additionally, that processes like rift obliquity (Agostini et al., 2009) and sediment supply can extend phases helps explain the large ranges of observed margin domain widths (e.g., 10 to 100 km for the necking domain, Chenin et al., 2017).

Though we find a broad correlation between deformation phases and rifted margin domains, there exist some interesting discrepancies. In our models there is no exposed continental mantle lithosphere (exhumation domain). Instead, hyperextension shifts directly into sediment-overlain asthenosphere exhumation (oceanic domain). In wide rifts, the fault network growth phase is greatly extended and the crust gradually thins over a large region (>122 km), as such distinguishing between the necking and hyperextension domain may be difficult. Rift migration creates a large region of hyper-extended crust that is translated from the margin in the direction of migration (left) to the opposite margin (Brune et al., 2014; Pérez-Gussinyé et al., 2020). This translation of sediment and crustal material fully overprints the remnant necking and hyperextended domains of the left margin, rendering the interpretation in terms of a single structural domain impossible.

627 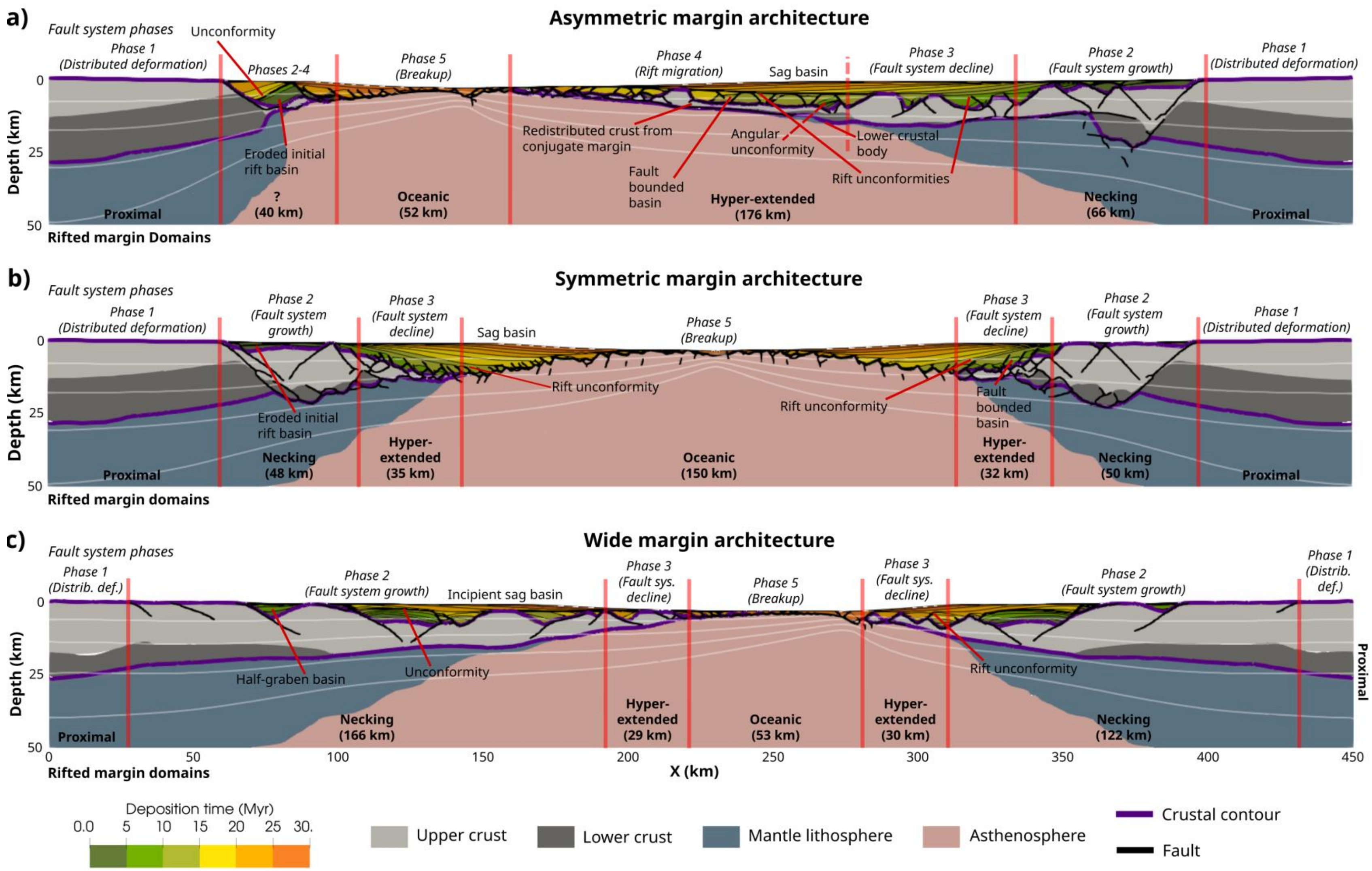

Figure 10. **Comparison of the margins at 30 Myr to structural domains, showing the similarities between the fault system deformation phase and structural domains. a) Asymmetric margins where deformation phases are indicated in italics on top, and structural domains in bold on bottom. Colored the rheology and deposition time. Extracted fault network is shown in black, and 50% crustal contour in purple. White temperature contours indicate 200, 400, 600, and 800 °C. b) Symmetric margin. c) Wide margin.**

5 Conclusions

We modeled the tectonic evolution of continental rifts and their interaction with surface processes to address three questions: 1) How do fault networks evolve in different rifts and rifted margins? 2) How are fault systems affected by surface process? 3) How do detachment faults and fault sequentiality evolve during rift migration?

We find that regardless of the rift type (e.g., asymmetric, symmetric, or wide) or the efficiency of surface processes, the active fault network properties such as length, displacement, and number of faults evolve according to five distinct phases that correspond to deformation domains: *phase 1: distributed deformation and coalescence* (proximal domain), *phase 2: fault growth* (necking), *phase 3: fault decline and basinward localization* (hyperextended), *phase 4: rift migration* (hyperextended, unique to asymmetric models), and *phase 5: continental breakup* (oceanic).

Our results suggest that surface processes do not drastically alter the overall rift evolution, but they do delay continental breakup. Similar to previous studies, we find that surface processes increase the lifespan of faults, which extends the fault growth phase. Deposition also enhances hyperextension and prolongs rift migration. We suggest that including surface processes has a stabilizing effect on faulting within models, resulting in less complex faulting patterns. An example of this is the reduced fault network complexity in phases 2 and 3, which suggests that sediment-starved margins exhibit greater fault network complexity in the early stages of rifting.

Our models show that rift migration is accommodated through frictional and viscous deformation in the exhumation channel, which creates a basal detachment fault that is rotated sub-horizontally, similar to the West Iberian S Reflector. Rooted in this channel, multiple normal faults form within a fault generation zone, where fault slip decreases with age and distance from this zone. The shallow parts of the exhumation channel satisfy the conditions for serpentinization, and we find that serpentinization is more likely in sediment-starved rift settings like the Iberian-Newfoundland margins, or the late stages of rift migration.

Acknowledgments, Samples, and Data

This study was conducted within the Helmholtz Young Investigators Group CRYSTALS (VH-NG-1132). We thank the Computational Infrastructure for Geodynamics (geodynamics.org), which is funded by the National Science Foundation under award EAR-0949446 and EAR-1550901, for supporting the development of ASPECT. The work was supported by the North-German Supercomputing Alliance (HLRN). Software and input files are found at https://doi.org/10.5281/zenodo.5753144. Figures were made using ParaView, colorscales from Crameri (2018) and Crameri et al., 2020, InkScape, and Python.

References

Agostini, A., Corti, G., Zeoli, A., and Mulugeta, G., 2009, Evolution, pattern, and partitioning of deformation during oblique continental rifting: Inferences from lithospheric-scale centrifuge models: Geochemistry, Geophysics, Geosystems, v. 10, doi:10.1029/2009GC002676.

Albaric, J., Déverchère, J., Petit, C., Perrot, J., and Le Gall, B., 2009, Crustal rheology and depth distribution of earthquakes: Insights from the central and southern East African Rift System:

Tectonophysics, v. 468, p. 28–41, doi:10.1016/J.TECTO.2008.05.021.

Albers, E., Bach, W., Pérez-Gussinyé, M., McCammon, C., and Frederichs, T., 2021, Serpentinization-Driven H2 Production From Continental Break-Up to Mid-Ocean Ridge Spreading: Unexpected High Rates at the West Iberia Margin: Frontiers in Earth Science, v. 9, p. 487, doi:10.3389/FEART.2021.673063/BIBTEX.

Andrés-Martínez, M., Pérez-Gussinyé, M., Armitage, J., and Morgan, J.P., 2019, Thermomechanical Implications of Sediment Transport for the Architecture and Evolution of Continental Rifts and Margins: Tectonics, v. 38, p. 641–665, doi:10.1029/2018TC005346.

Armitage, J.J., Dunkley Jones, T., Duller, R.A., Whittaker, A.C., and Allen, P.A., 2013, Temporal buffering of climate-driven sediment flux cycles by transient catchment response: Earth and Planetary Science Letters, v. 369–370, p. 200–210, doi:10.1016/J.EPSL.2013.03.020.

Artemieva, I.M., 2006, Global 1° × 1° thermal model TC1 for the continental lithosphere: Implications for lithosphere secular evolution: Tectonophysics, v. 416, p. 245–277, doi:10.1016/j.tecto.2005.11.022.

Bahadori, A., and Holt, W.E., 2019, Geodynamic evolution of southwestern North America since the Late Eocene: Nature Communications, v. 10, p. 5213, doi:10.1038/s41467-019-12950-8.

Bayrakci, G. et al., 2016, Fault-controlled hydration of the upper mantle during continental rifting: Nature Geoscience 2016 9:5, v. 9, p. 384–388, doi:10.1038/ngeo2671.

Beucher, R., and Huismans, R.S., 2020, Morphotectonic Evolution of Passive Margins Undergoing Active Surface Processes: Large-Scale Experiments Using Numerical Models: Geochemistry, Geophysics, Geosystems, v. 21, doi:10.1029/2019GC008884.

Bickert, M., Lavier, L., and Cannat, M., 2020, How do detachment faults form at ultraslow mid-ocean ridges in a thick axial lithosphere? Earth and Planetary Science Letters, v. 533, p. 116048, doi:10.1016/J.EPSL.2019.116048.

Braun, J., and Willett, S.D., 2013, A very efficient O(n), implicit and parallel method to solve the stream power equation governing fluvial incision and landscape evolution: Geomorphology, v. 180–181, p. 170–179, doi:10.1016/J.GEOMORPH.2012.10.008.

Brune, S., Heine, C., Clift, P.D., and Pérez-Gussinyé, M., 2017, Rifted margin architecture and crustal rheology: Reviewing Iberia-Newfoundland, Central South Atlantic, and South China Sea: Marine and Petroleum Geology, v. 79, p. 257–281, doi:10.1016/j.marpetgeo.2016.10.018.

Brune, S., Heine, C., Pérez-Gussinyé, M., and Sobolev, S. V., 2014, Rift migration explains continental margin asymmetry and crustal hyper-extension: Nature Communications, v. 5, p. 1–9, doi:10.1038/ncomms5014.

Buck, W.R., 1988, flexural rotation of normal faults: Tectonics, v. 7, p. 959–973, doi:10.1029/TC007I005P00959.

Buck, W.R., Lavier, L.L., and Poliakov, A.N.B., 1999, How to make a rift wide: Phil. Trans. R. Soc., v. A. 357, p. 671–693.

Buiter, S.J.H., 2021, A discussion on how, when and where surface processes interplay with extensional tectonic deformation: EGU General Assembly 2021, v. EGU21-8665, doi:https://doi.org/10.5194/egusphere-egu21-8665.

Buiter, S.J.H., Huismans, R.S., and Beaumont, C., 2008, Dissipation analysis as a guide to mode selection during crustal extension and implications for the styles of sedimentary basins: Journal of Geophysical Research: Solid Earth, v. 113, doi:10.1029/2007JB005272.

Chenin, P., Manatschal, G., Decarlis, A., Schmalholz, S.M., Duretz, T., and Beltrando, M., 2019, Emersion of Distal Domains in Advanced Stages of Continental Rifting Explained by Asynchronous Crust and Mantle Necking: Geochemistry, Geophysics, Geosystems, v. 20, p. 3821–3840, doi:https://doi.org/10.1029/2019GC008357.

Chenin, P., Manatschal, G., Ghienne, J.-F.J.-F., and Chao, P., 2021, The syn-rift tectono-stratigraphic record of rifted margins (Part II): A new model to break through the proximal/distal interpretation frontier: Basin Research, v. 00, p. 1–44, doi:10.1111/bre.12628.

Chenin, P., Manatschal, G., Picazo, S., Müntener, O., Karner, G., Johnson, C., and Ulrich, M., 2017, Influence of the architecture of magma-poor hyperextended rifted margins on orogens produced by the closure of narrow versus wide oceans: Geosphere, v. 13, p. 559–576, doi:10.1130/GES01363.1.

Choi, E., Buck, W.R., Lavier, L.L., and Petersen, K.D., 2013, Using core complex geometry to constrain fault strength: Geophysical Research Letters, v. 40, p. 3863–3867, doi:10.1002/GRL.50732.

Clerc, C., Ringenbach, J.C., Jolivet, L., and Ballard, J.F., 2018, Rifted margins: Ductile deformation, boudinage, continentward-dipping normal faults and the role of the weak lower crust: Gondwana Research, v. 53, p. 20–40, doi:10.1016/J.GR.2017.04.030.

Corti, G., 2012, Evolution and characteristics of continental rifting: Analog modeling-inspired view and comparison with examples from the East African Rift System: Tectonophysics, v. 522–523, p. 1–33, doi:10.1016/j.tecto.2011.06.010.

Crameri, F., 2018, Scientific colour maps. Zenodo.:, doi:http://doi.org/10.5281/zenodo.1243862.

Crameri, F., Shephard, G.E., and Heron, P.J., 2020, The misuse of colour in science communication: Nature Communications 2020 11:1, v. 11, p. 1–10, doi:10.1038/s41467-020-19160-7.

Densmore, A.L., Allen, P.A., and Simpson, G., 2007, Development and response of a coupled catchment fan system under changing tectonic and climatic forcing: Journal of Geophysical Research: Earth Surface, v. 112, p. 1002, doi:10.1029/2006JF000474.

Depolo, C.M., and Anderson, J.G., 2000, Estimating the slip rates of normal faults in the Great Basin, USA: Basin Research, v. 12, p. 227–240, doi:10.1111/J.1365-2117.2000.00131.X.

Ebinger, C., and Scholz, C.A., 2012, Continental Rift Basins: The East African Perspective, *in* Tectonics of Sedimentary Basins: Recent Advances, John Wiley & Sons, Ltd, p. 183–208, doi:10.1002/9781444347166.ch9.

Emmanuel, S., and Berkowitz, B., 2006, Suppression and stimulation of seafloor hydrothermal convection by exothermic mineral hydration: Earth and Planetary Science Letters, v. 243, p. 657–668, doi:10.1016/J.EPSL.2006.01.028.

Gassmöller, R., Lokavarapu, H., Heien, E., Puckett, E.G., and Bangerth, W., 2018, Flexible and Scalable Particle-in-Cell Methods With Adaptive Mesh Refinement for Geodynamic Computations: Geochemistry, Geophysics, Geosystems, v. 19, p. 3596–3604, doi:10.1029/2018GC007508.

Gawthorpe, R.L., and Leeder, M.R., 2000, Tectono-sedimentary evolution of active extensional basins: Basin Research, v. 12, p. 195–218, doi:10.1111/J.1365-2117.2000.00121.X.

Glerum, A., Thieulot, C., Fraters, M., Blom, C., and Spakman, W., 2018, Nonlinear viscoplasticity in ASPECT: Benchmarking and applications to subduction: Solid Earth, v. 9, p. 267–294, doi:10.5194/se-9-267-2018.

Goldsworthy, M., and Jackson, J., 2001, Migration of activity within normal fault systems: examples from the Quaternary of mainland Greece: Journal of Structural Geology, v. 23, p. 489–506, doi:10.1016/S0191-8141(00)00121-8.

Guerit, L., Yuan, X.P., Carretier, S., Bonnet, S., Rohais, S., Braun, J., and Rouby, D., 2019, Fluvial landscape evolution controlled by the sediment deposition coefficient: Estimation from experimental and natural landscapes: Geology, v. 47, p. 853–856, doi:10.1130/G46356.1.

Guo, Z., and Hall, R.W., 1992, Fast fully parallel thinning algorithms: CVGIP: Image Understanding, v. 55, p. 317–328, doi:10.1016/1049-9660(92)90029-3.

Heine, C., Zoethout, J., and Müller, R.D., 2013, Kinematics of the South Atlantic rift: Solid Earth, v. 4, p. 215–253, doi:10.5194/se-4-215-2013.

Heister, T., Dannberg, J., Gassmöller, R., and Bangerth, W., 2017, High Accuracy Mantle Convection Simulation through Modern Numerical Methods – II: Realistic Models and Problems.: Geophysical Journal International, v. 210, p. 833–851, doi:doi:10.1093/gji/ggx195.

Heron, P.J., Peace, A.L., McCaffrey, K.J.W., Welford, J.K., Wilson, R., van Hunen, J., and Pysklywec, R.N., 2019, Segmentation of Rifts Through Structural Inheritance: Creation of the Davis Strait: Tectonics, v. 38, p. 2411–2430, doi:10.1029/2019TC005578.

Hirth, G., and Kohlstedt, D., 2003, Rheology of the upper mantle and the mantle wedge: a view from the experimentalists: Inside the Subudction Factory Geophysical Monograph (American Geophysical Union), v. 183.

Hoffmann, H.J., and Reston, T.J., 1992, Nature of the S reflector beneath the Galicia Banks rifted margin: preliminary results from prestack depth migration: Geology, v. 20, p. 1091–1094, doi:10.1130/0091-7613(1992)020<1091:NOTSRB>2.3.CO;2.

Huismans, R.S., and Beaumont, C., 2014, Rifted continental margins: The case for depth-dependent extension: Earth and Planetary Science Letters, v. 407, p. 148–162, doi:10.1016/J.EPSL.2014.09.032.

Huismans, R.S., and Beaumont, C., 2003, Symmetric and asymmetric lithospheric extension: Relative effects of frictional-plastic and viscous strain softening: Journal of Geophysical

Research: Solid Earth, v. 108, p. 1–22, doi:10.1029/2002jb002026.

Jammes, S., and Lavier, L.L., 2016, The effect of bimineralic composition on extensional processes at lithospheric scale: Geochemistry, Geophysics, Geosystems, v. 17, p. 3375–3392, doi:10.1002/2016GC006399.

Jolie, E. et al., 2021, Geological controls on geothermal resources for power generation: Nature Reviews Earth & Environment 2021 2:5, v. 2, p. 324–339, doi:10.1038/s43017-021-00154-y.

Karato, S., and Wu, P., 1993, Rheology the Upper Mantle : Synthesis: v. 260.

Kronbichler, M., Heister, T., and Bangerth, W., 2012, High Accuracy Mantle Convection Simulation through Modern Numerical Methods.: Geophysical Journal International, v. 191, doi:doi:10.1111/j.1365-246x.2012.05609.x.

Lavier, L.L., and Manatschal, G., 2006, A mechanism to thin the continental lithosphere at magma-poor margins: Nature, v. 440, p. 324–328, doi:10.1038/nature04608.

Leeder, M.R., and Gawthorpe, R.L., 1987, Sedimentary models for extensional tilt-block/half-graben basins: Geological Society, London, Special Publications, v. 28, p. 139 LP – 152, doi:10.1144/GSL.SP.1987.028.01.11.

Lefeuvre, N., Truche, L., Donzé, F.V., Ducoux, M., Barré, G., Fakoury, R.A., Calassou, S., and Gaucher, E.C., 2021, Native H2 Exploration in the Western Pyrenean Foothills: Geochemistry, Geophysics, Geosystems, v. 22, p. e2021GC009917, doi:10.1029/2021GC009917.

Lymer, G., Cresswell, D.J.F., Reston, T.J., Bull, J.M., Sawyer, D.S., Morgan, J.K., Stevenson, C., Causer, A., Minshull, T.A., and Shillington, D.J., 2019, 3D development of detachment faulting during continental breakup: Earth and Planetary Science Letters, v. 515, p. 90–99, doi:10.1016/j.epsl.2019.03.018.

Maniatis, G., Kurfeß, D., Hampel, A., and Heidbach, O., 2009, Slip acceleration on normal faults due to erosion and sedimentation - Results from a new three-dimensional numerical model coupling tectonics and landscape evolution: Earth and Planetary Science Letters, v. 284, p. 570–582, doi:10.1016/J.EPSL.2009.05.024.

Martin, Y., 2000, Modelling hillslope evolution: linear and nonlinear transport relations: Geomorphology, v. 34, p. 1–21, doi:10.1016/S0169-555X(99)00127-0.

McDermott, K., and Reston, T., 2015, To see, or not to see? Rifted margin extension: Geology, v. 43, p. 967–970, doi:10.1130/G36982.1.

Muirhead, J.D., Kattenhorn, S.A., Lee, H., Mana, S., Turrin, B.D., Fischer, T.P., Kianji, G., Dindi, E., and Stamps, D.S., 2016, Evolution of upper crustal faulting assisted by magmatic volatile release during early-stage continental rift development in the East African Rift: Geosphere, v. 12, p. 1670–1700, doi:10.1130/GES01375.1.

Muldashev, I.A., Pérez-Gussinyé, M., and de Araújo, M.N.C., 2021, KineDyn: Thermomechanical forward method for validation of seismic interpretations and investigation of dynamics of rifts and rifted margins: Physics of the Earth and Planetary Interiors, v. 317, p. 106748, doi:10.1016/J.PEPI.2021.106748.

Nagel, T.J., and Buck, W.R., 2004, Symmetric alternative to asymmetric rifting models: Geology, v. 32, p. 937–940, doi:10.1130/G20785.1.

Naliboff, J.B., Buiter, S.J.H., Péron-Pinvidic, G., Osmundsen, P.T., and Tetreault, J., 2017, Complex fault interaction controls continental rifting: Nature Communications, v. 8, doi:10.1038/S41467-017-00904-X.

Naliboff, J.B., Glerum, A., Brune, S., Péron-Pinvidic, G., and Wrona, T., 2020, Development of 3-D Rift Heterogeneity Through Fault Network Evolution: Geophysical Research Letters, v. 47, p. e2019GL086611, doi:https://doi.org/10.1029/2019GL086611.

Neuharth, D., Brune, S., Glerum, A., Morley, C.K., Yuan, X.P., and Braun, J., 2021, Flexural strike-slip basins: GEOLOGY,.

Olive, J.-A.A., Behn, M.D., and Malatesta, L.C., 2014, Modes of extensional faulting controlled by surface processes: Geophysical Research Letters, v. 41, p. 6725–6733, doi:https://doi.org/10.1002/2014GL061507.

Pasyanos, M.E., Masters, T.. G., Laske, G., and Ma, Z., 2014, LITH1.0: An updated crust and lithospheric model of the Earth: Journal of Geophysical Research: Solid Earth, v. 119, p. 2153–2173, doi:10.1002/2014JB011376.Received.

Pérez-Gussinyé, M., Andrés-Martínez, M., Araújo, M., Xin, Y., Armitage, J., and Morgan, J.P., 2020, Lithospheric Strength and Rift Migration Controls on Synrift Stratigraphy and Breakup Unconformities at Rifted Margins: Examples From Numerical Models, the Atlantic and South China Sea Margins: Tectonics, v. 39, p. e2020TC006255, doi:10.1029/2020TC006255.

Pérez-Gussinyé, M., Morgan, J.P., Reston, T.J., and Ranero, C.R., 2006, The rift to drift transition at non-volcanic margins: Insights from numerical modelling: Earth and Planetary Science Letters, v. 244, p. 458–473, doi:10.1016/J.EPSL.2006.01.059.

Pérez-Gussinyé, M., Reston, T.J., and Morgan, J.P., 2001, Serpentinization and magmatism during extension at non-volcanic margins: The effect of initial lithospheric structure: Geological Society Special Publication, v. 187, p. 551–576, doi:10.1144/GSL.SP.2001.187.01.27.

Peron-Pinvidic, G., Manatschal, G., and Osmundsen, P.T., 2013, Structural comparison of archetypal Atlantic rifted margins: A review of observations and concepts: Marine and Petroleum Geology, v. 43, p. 21–47.

Ranero, C.R., and Pérez-Gussinyé, M., 2010, Sequential faulting explains the asymmetry and extension discrepancy of conjugate margins: Nature, v. 468, p. 294–299, doi:10.1038/NATURE09520.

Reston, T.J., 2010, The opening of the central segment of the South Atlantic: Symmetry and the extension discrepancy: Petroleum Geoscience, v. 16, p. 199–206, doi:10.1144/1354-079309-907.

Reston, T.J., Booth-Rea, G., Leythaeuser, T., Sawyer, D., Klaeschen, D., and Long, C., 2007, Movement along a low-angle normal fault: The S reflector west of Spain: Geochemistry, Geophysics, Geosystems, v. 8, doi:10.1029/2006GC001437.

Reston, T.J., and Pérez-Gussinyé, M., 2007, Lithospheric extension from rifting to continental breakup at magma-poor margins: Rheology, serpentinisation and symmetry: International Journal of Earth Sciences, v. 96, p. 1033–1046, doi:10.1007/S00531-006-0161-Z/FIGURES/9.

Richter, M.J.E.A., Brune, S., Riedl, S., Glerum, A., Neuharth, D., and Strecker, M.R., 2021, Controls on Asymmetric Rift Dynamics: Numerical Modeling of Strain Localization and Fault Evolution in the Kenya Rift: Tectonics, v. 40, p. e2020TC006553, doi:10.1029/2020TC006553.

Rose, I., Buffett, B., and Heister, T., 2017, Stability and Accuracy of Free Surface Time Integration in Viscous Flows.: Physics of the Earth and Planetary Interiors, v. 262, p. 90–100, doi:doi:10.1016/j.pepi.2016.11.007.

Rouby, D., Braun, J., Robin, C., Dauteuil, O., and Deschamps, F., 2013, Long-term stratigraphic evolution of Atlantic-type passive margins: A numerical approach of interactions between surface processes, flexural isostasy and 3D thermal subsidence: Tectonophysics, v. 604, p. 83–103, doi:10.1016/j.tecto.2013.02.003.

Rutter, E.H., and Brodie, K.H., 2004, Experimental grain size-sensitive flow of hot-pressed Brazilian quartz aggregates: Journal of Structural Geology, v. 26, p. 2011–2023, doi:10.1016/j.jsg.2004.04.006.

Rybacki, E., Gottschalk, M., Wirth, R., and Dresen, G., 2006, Influence of water fugacity and activation volume on the flow properties of fine-grained anorthite aggregates: Journal of Geophysical Research: Solid Earth, v. 111, doi:10.1029/2005JB003663.

Scholz, C.H., 2019, The mechanics of earthquakes and faulting: Cambridge university press.

Sibuet, J.C., 1992, New constraints on the formation of the non-volcanic continental Galicia–Flemish Cap conjugate margins: Journal of the Geological Society, v. 149, p. 829–840, doi:10.1144/GSJGS.149.5.0829.

Stern, R.J., and Johnson, P.R., 2019, Constraining the Opening of the Red Sea: Evidence from the Neoproterozoic Margins and Cenozoic Magmatism for a Volcanic Rifted Margin: Geological Setting, Palaeoenvironment and Archaeology of the Red Sea, p. 53–79, doi:10.1007/978-3-319-99408-6_4.

Stock, J.D., and Montgomery, D.R., 1999, Geologic constraints on bedrock river incision using the stream power law: Journal of Geophysical Research: Solid Earth, v. 104, p. 4983–4993.

Tetreault, J.L., and Buiter, S.J.H., 2018, The influence of extension rate and crustal rheology on the evolution of passive margins from rifting to break-up: Tectonophysics, v. 746, p. 155–172, doi:10.1016/j.tecto.2017.08.029.

Theunissen, T., and Huismans, R.S., 2019, Long-Term Coupling and Feedback Between Tectonics and Surface Processes During Non-Volcanic Rifted Margin Formation: Journal of Geophysical Research: Solid Earth, v. 124, p. 12323–12347, doi:10.1029/2018JB017235.

Whipple, K.X., and Tucker, G.E., 1999, Dynamics of the stream-power river incision model: Implications for height limits of mountain ranges, landscape response timescales, and research needs: Journal of Geophysical Research: Solid Earth, v. 104, p. 17661–17674.

Whitmarsh, R.B., Manatschal, G., and Minshull, T.A., 2001, Evolution of magma-poor continental margins from rifting to seafloor spreading: Nature 2001 413:6852, v. 413, p. 150–154, doi:10.1038/35093085.

Wilkinson, J.J., 2014, Sediment-Hosted Zinc–Lead Mineralization: Processes and Perspectives: Treatise on Geochemistry: Second Edition, v. 13, p. 219–249, doi:10.1016/B978-0-08-095975-7.01109-8.

Williams, J.N., Fagereng, Å., Wedmore, L.N.J., Biggs, J., Mphepo, F., Dulanya, Z., Mdala, H., and Blenkinsop, T., 2019, How Do Variably Striking Faults Reactivate During Rifting? Insights From Southern Malawi: Geochemistry, Geophysics, Geosystems, v. 20, p. 3588–3607, doi:10.1029/2019GC008219.

Wolf, S.G., Huismans, R.S., Muñoz, J.A., Curry, M.E., and van der Beek, P., 2021, Growth of Collisional Orogens From Small and Cold to Large and Hot—Inferences From Geodynamic Models: Journal of Geophysical Research: Solid Earth, v. 126, p. e2020JB021168, doi:10.1029/2020JB021168.

Wu, K., Otoo, E., and Suzuki, K., 2009, Optimizing two-pass connected-component labeling algorithms: Pattern Analysis and Applications, v. 12, p. 117–135, doi:10.1007/S10044-008-0109-Y/FIGURES/8.

Yuan, X.P., Braun, J., Guerit, L., Rouby, D., and Cordonnier, G., 2019a, A New Efficient Method to Solve the Stream Power Law Model Taking Into Account Sediment Deposition: Journal of Geophysical Research: Earth Surface, v. 124, p. 1346–1365, doi:10.1029/2018JF004867.

Yuan, X.P., Braun, J., Guerit, L., Simon, B., Bovy, B., Rouby, D., Robin, C., and Jiao, R., 2019b, Linking continental erosion to marine sediment transport and deposition: A new implicit and O(N) method for inverse analysis: Earth and Planetary Science Letters, v. 524, p. 115728, doi:10.1016/j.epsl.2019.115728.

Zwaan, F., Schreurs, G., and Adam, J., 2018, Effects of sedimentation on rift segment evolution and rift interaction in orthogonal and oblique extensional settings: Insights from analogue models analysed with 4D X-ray computed tomography and digital volume correlation techniques: Global and Planetary Change, v. 171, p. 110–133, doi:10.1016/j.gloplacha.2017.11.002.

AGU PUBLICATIONS

Tectonics

Supporting Information for

Evolution of rift systems and their fault networks in response to surface processes

Derek Neuharth[1,2], Sascha Brune[1,2], Thilo Wrona[1], Anne Glerum[1], Jean Braun[1,2], Xiaoping Yuan[3,1]

[1]GFZ German Research Centre for Geosciences, Telegrafenberg, 14473 Potsdam, Germany.

[2]Institute of Geosciences, University of Potsdam, Germany.

[3]School of Earth Sciences, China University of Geosciences, Wuhan, China

Contents of this file

Figure S1
Figure S2
Figure S3
Figure S4
Figure S5
Figure S6
Figure S7
Table S1
Table S2
Table S3

Additional Supporting Information (Files uploaded separately)

Captions for Movies S1 to S6

Introduction

In this supplementary material, we provide 3 tables detailing the parameters for setting up the ASPECT model (Table S1), FastScape model (Table S2), and for the different phase timings (Table S3). We include 7 figures that compare the x-extension held on the tracked fault system along a depth contour to the extension prescribed as a boundary condition (Fig. S1), the amount of fault slip held on active faults vs. the entire fault system, as well as information on how the graphs were processed (Fig. S2), and comparisons on the number of faults in the system over time for different models (Fig. S3, S4, S5, and S7). We additionally include 2 animations for each rift type, where one animation shows the surface processes model with the tectonic model (Video S1, S3, and S5) and the other shows the tracked fault system overlying the tectonic model (Video S2, S4, and S6).

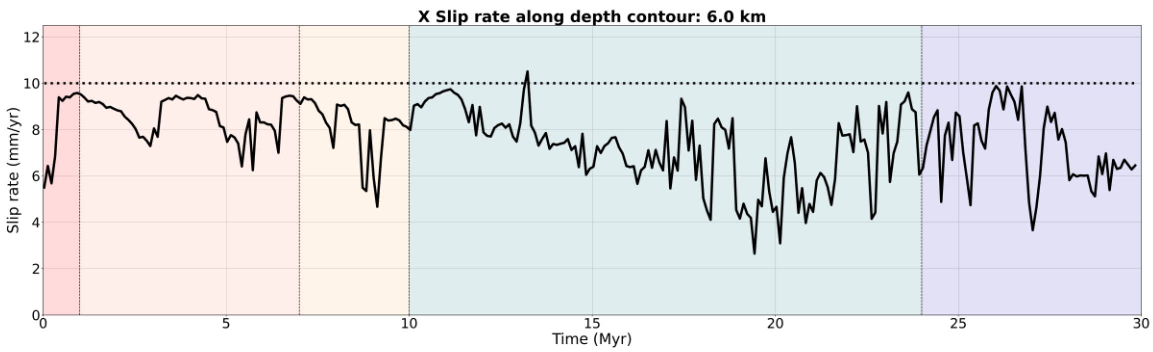

Figure S1. Figure comparing extension held on the tracked fault system vs. the amount of extension prescribed by the boundary conditions. The dashed line at 10 mm/yr represents the extension prescribed at the model boundaries. The solid black line shows the cumulative extension (X slip rate) of all faults along the 6 km depth contour. In an idealized model where all deformation is accommodated by major faults, both lines should coincide. Practically, however, there is a varying degree of deformation that is accommodated within fault blocks and in small faults that are not accounted for by the analysis. This comparison illustrates that deformation is localized on major faults during phase 2 and 3, while the other phases involve a larger degree of off-fault deformation.

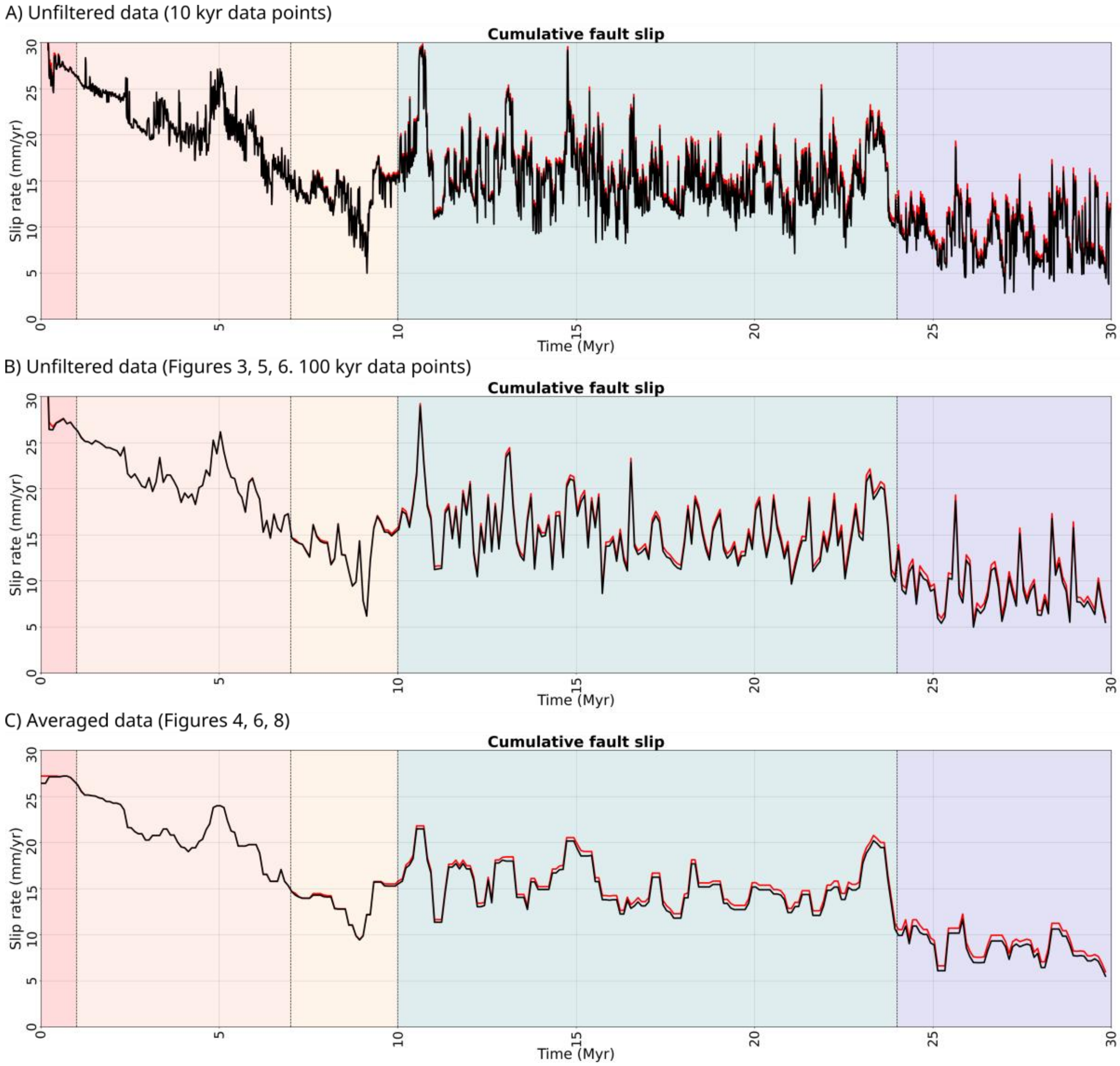

Figure S2. Comparison between the cumulative total slip held by all tracked faults (red) vs. the cumulative total slip held by the active faults (black). When plotting the fault property evolution in a time series the values may change rapidly because of our approach to employ thresholds on fault size and plastic strain. To reduce the noise and increase graph readability, the graphs are post-processed in a way that does not affect the presented results. First, all graphs are plotted at 100 kyr intervals. Second, when plotting active fault properties, for a fault to be considered active it had to be active the previous timestep (10 kyr earlier) as well as the current timestep. To showcase how our processing affects the results: A) Plotting every 10 kyr data point available. B) Plotting data every 100 kyr, such as in figures 3, 5, 7, and S1. C) Averaging the 100 kyr points from B over 5 points (500 kyr), such as in figures 4, 6, 8, S3, S4, S5, and S6.

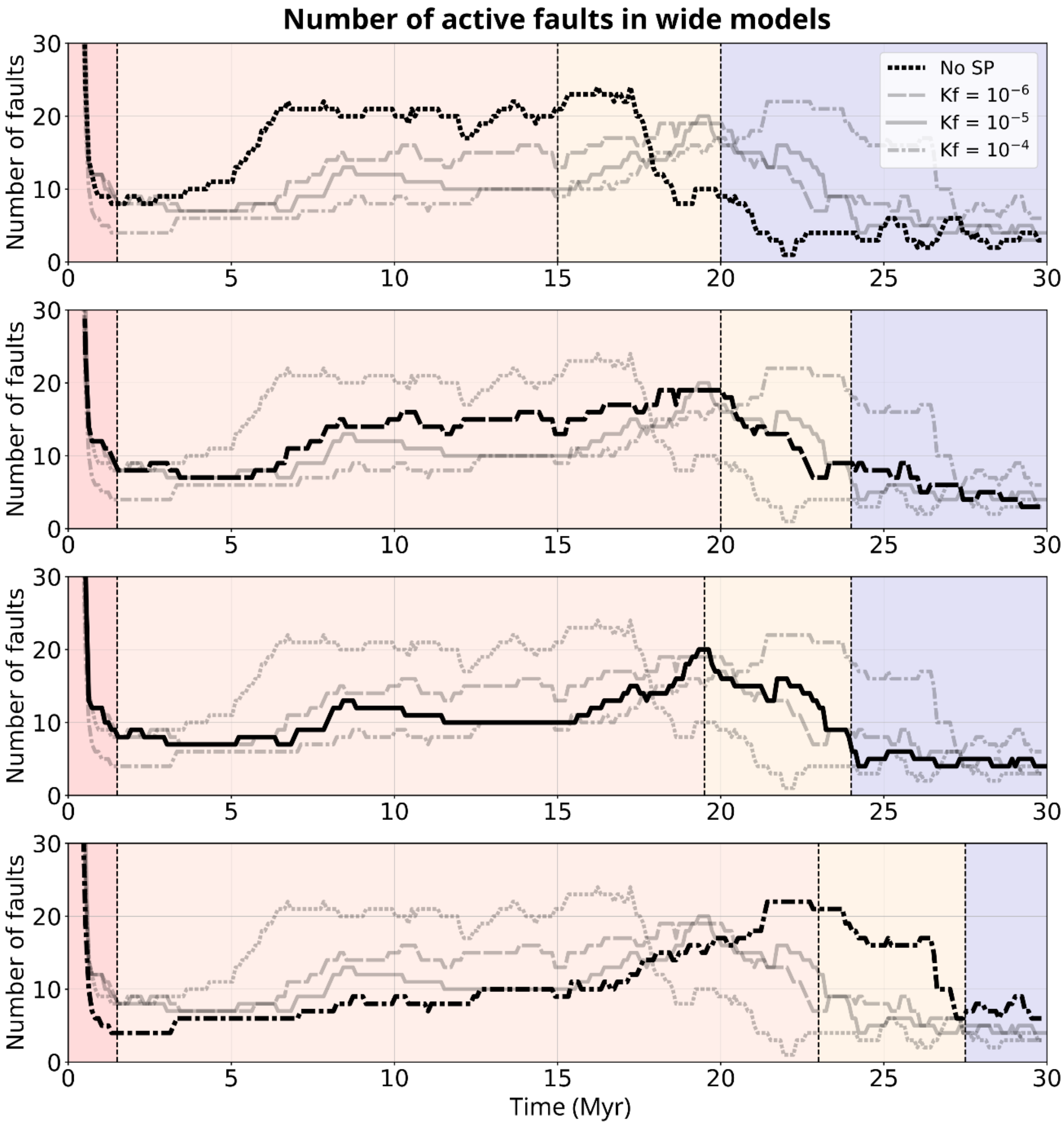

Figure S3. Number of active faults in wide rift models with varying levels of sedimentation. Phases are indicated by colors, with phase 1 (red), phase 2 (orange), phase 3 (yellow), and phase 5 (purple).

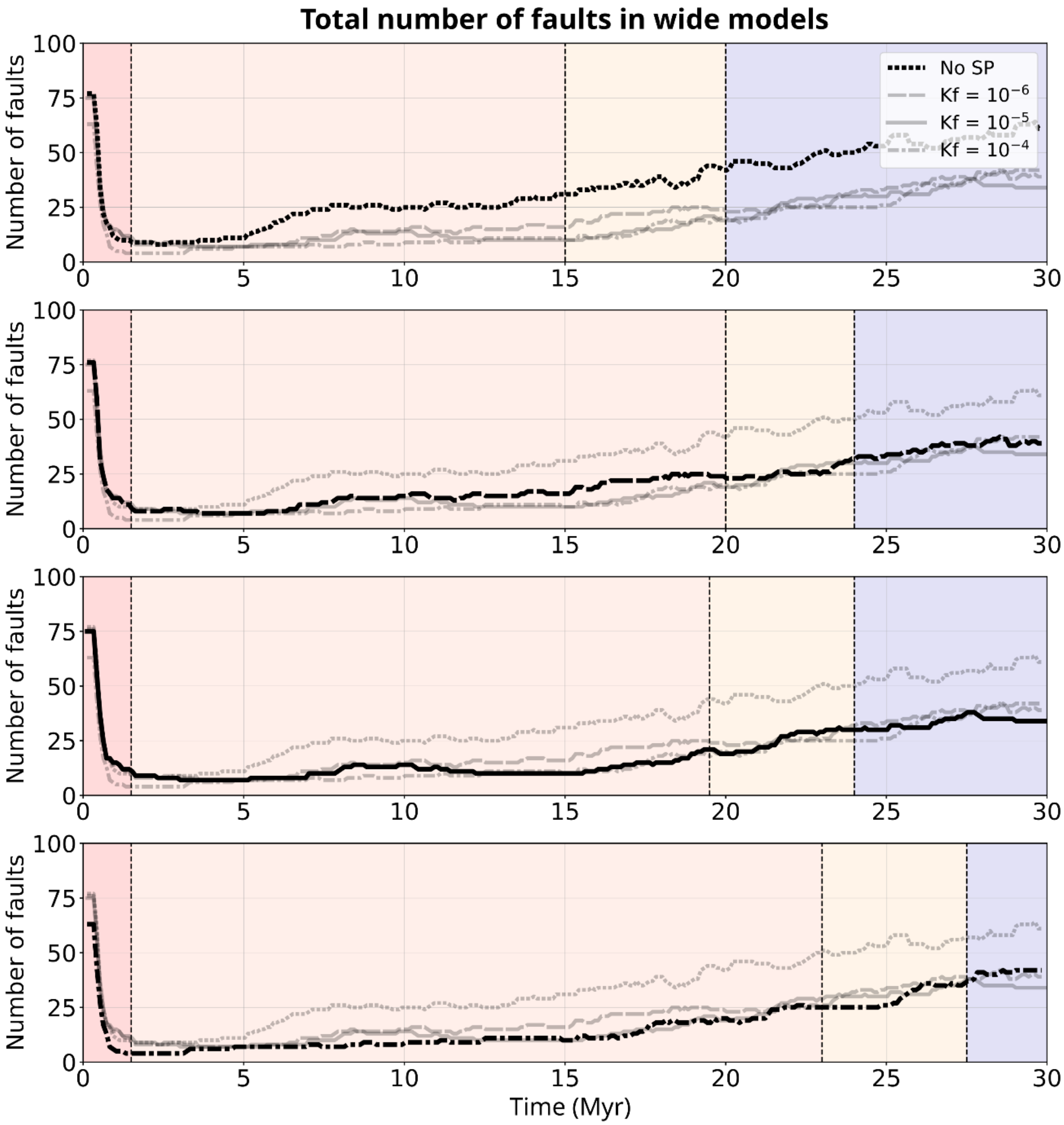

Figure S4. Total number of faults in wide rift models with varying levels of sedimentation. Includes active and inactive faults. Phases are indicated by colors, with phase 1 (red), phase 2 (orange), phase 3 (yellow), and phase 5 (purple).

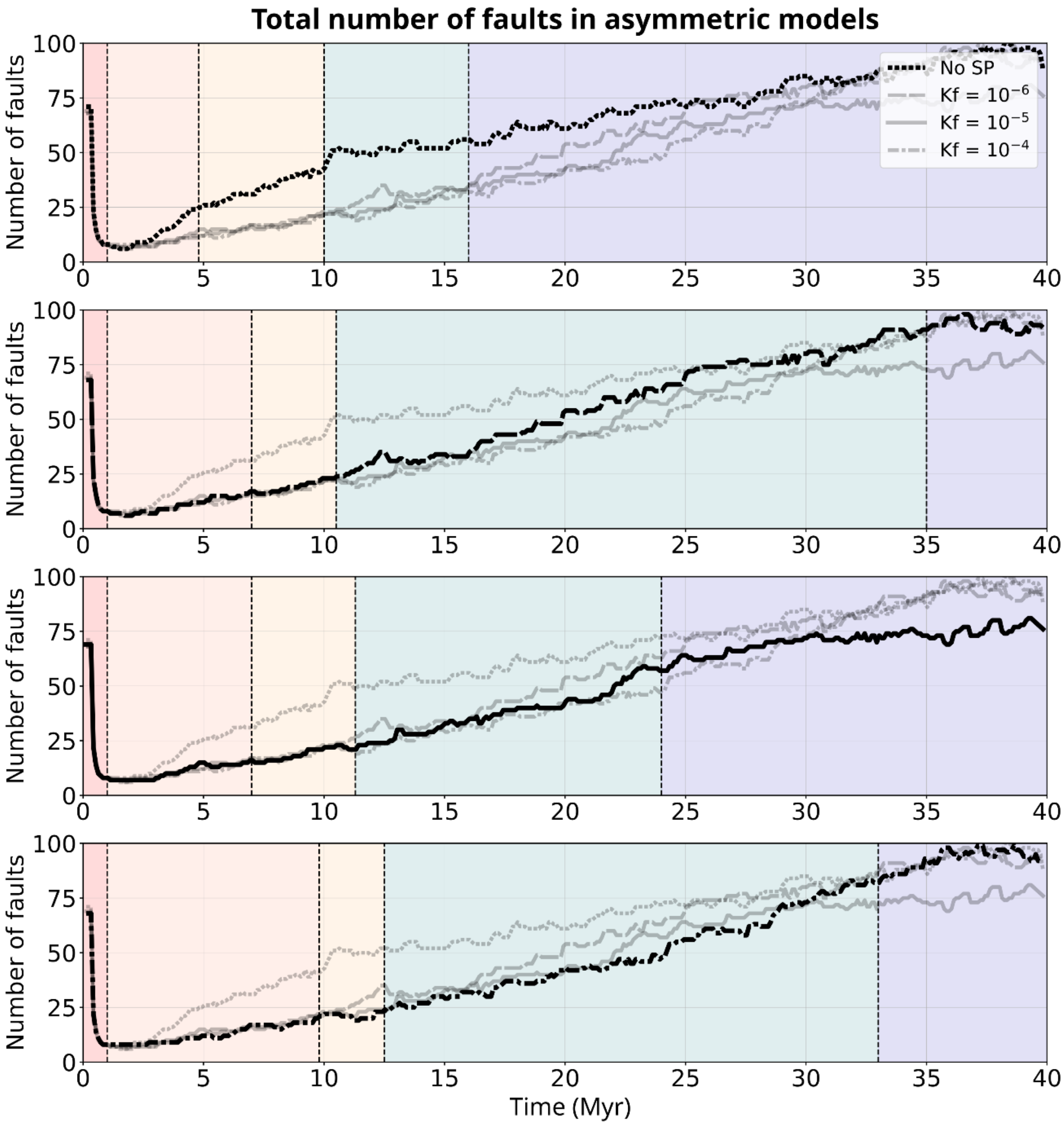

Figure S5. Total number of faults in asymmetric rift models with varying levels of sedimentation. Includes active and inactive faults. Phases are indicated by colors, with phase 1 (red), phase 2 (orange), phase 3 (yellow), and phase 5 (purple).

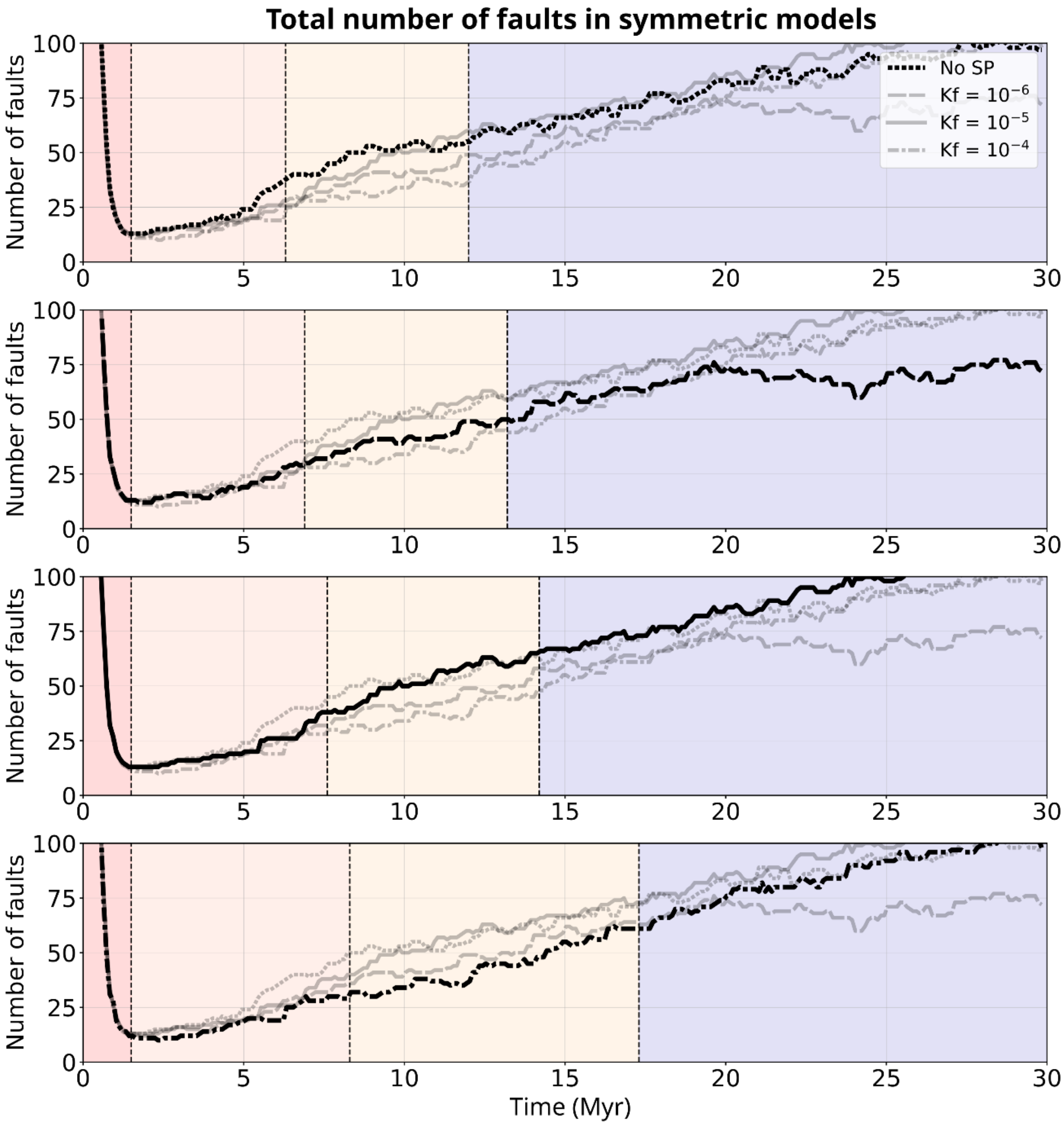

Figure S6. Total number of faults in symmetric rift models with varying levels of sedimentation. Includes active and inactive faults. Phases are indicated by colors, with phase 1 (red), phase 2 (orange), phase 3 (yellow), phase 4 (green) and phase 5 (purple).

Parameter	Symbol	Units	Sediment	Upper crust	Lower crust	Lithospheric mantle	Asthenosphere
Reference surface density*	ρ_0	kgm^{-3}	2520	2700	2850	3280	3300
Thermal expansivity	α	K^{-1}	$3.7{\cdot}10^{-5}$	$2.7{\cdot}10^{-5}$	$2.7{\cdot}10^{-5}$	$3.0{\cdot}10^{-5}$	$3.0{\cdot}10^{-5}$
Thermal diffusivity	κ	m^2 s^{-1}	$7.28{\cdot}10^{-7}$	$7.72{\cdot}10^{-7}$	$7.31{\cdot}10^{-7}$	$8.38{\cdot}10^{-7}$	$8.33{\cdot}10^{-7}$
Heat capacity	C_p	J kg^{-1} K^{-1}	1200	1200	1200	1200	1200
Heat production	H	W m^{-3}	$1.2{\cdot}10^{-6}$	$1.0{\cdot}10^{-6}$	$0.1{\cdot}10^{-6}$	0	0
Cohesion	C	Pa	$5{\cdot}10^6$	$5{\cdot}10^6$	$5{\cdot}10^6$	$5{\cdot}10^6$	$5{\cdot}10^6$
Internal friction angle (unweakened)	ϕ	°	26.56	26.56	26.56	26.56	26.56
Plastic strain weakening interval	-	-	[0,1]	[0,1]	[0,1]	[0,1]	[0,1]
Plastic strain weakening factor	ϕ_{wf}	-	0.25	0.25	0.25	0.25	0.25
Viscous strain weakening interval	-	-	[0,1]	[0,1]	[0,1]	[0,1]	[0,1]
Viscous strain weakening factor	-	-	0.25	0.25	0.25	0.25	1.0
Creep properties			***Wet quartzite***	***Wet quartzite***	***Wet anorthite***	***Dry olivine***	***Wet olivine***
Stress exponent (dis)	n	-	4.0	4.0	3.0	3.5	3.5
Constant prefactor (dis)	A_{dis}	Pa^{-n}s^{-1}	$8.57{\cdot}10^{-28}$	$8.57{\cdot}10^{-28}$	$7.13{\cdot}10^{-18}$	$6.52{\cdot}10^{-16}$	$2.12{\cdot}10^{-15}$
Activation energy (dis)	E_{dis}	Jmol^{-1}	$223{\cdot}10^3$	$223{\cdot}10^3$	$345{\cdot}10^3$	$530{\cdot}10^3$	$480{\cdot}10^3$
Activation volume (dis)	V_{dis}	m^3 mol^{-1}	0	0	$38{\cdot}10^{-6}$	$18{\cdot}10^{-6}$	$11{\cdot}10^{-6}$
Constant prefactor (diff)	A_{diff}	Pa^{-1}s^{-1}	$5.79{\cdot}10^{-19}$	$5.79{\cdot}10^{-19}$	$2.99{\cdot}10^{-25}$	$2.25{\cdot}10^{-9}$	$1.5{\cdot}10^{-9}$
Activation energy (diff)	E_{diff}	Jmol^{-1}	$223{\cdot}10^3$	$223{\cdot}10^3$	$159{\cdot}10^3$	$375{\cdot}10^3$	$335{\cdot}10^3$
Activation volume (diff)	V_{diff}	m^3 mol^{-1}	0	0	$38{\cdot}10^{-6}$	$6{\cdot}10^{-6}$	$4{\cdot}10^{-6}$
Grain size (diff)	d	m	0.001	0.001	0.001	0.001	0.001
Grain size exponent (diff)	m	-	2.0	2.0	3.0	0	0

Table S1. Reference parameter values. dis – dislocation creep. diff – diffusion creep. *Model input densities are scaled so that at surface temperatures (273 K) these values are reached.

<table>
<tr><th>Parameter</th><th>Symbol</th><th>Unit</th><th colspan="3">Value</th></tr>
<tr><td>Drainage area exponent</td><td>m</td><td>-</td><td colspan="3">0.4</td></tr>
<tr><td>Slope exponent</td><td>n</td><td>-</td><td colspan="3">1</td></tr>
<tr><td>Bedrock/sediment diffusivity</td><td>K_c</td><td>m^2/yr</td><td colspan="3">$5 \cdot 10^{-3}$</td></tr>
<tr><td>Bedrock/sediment erodibility</td><td>K_f</td><td>$m^{0.2}/yr$</td><td colspan="3">$1 \cdot 10^{-4}$, $1 \cdot 10^{-5}$, or $1 \cdot 10^{-6}$</td></tr>
<tr><td>Bedrock/sediment deposition coefficient</td><td>G</td><td>-</td><td colspan="3">1</td></tr>
<tr><td>Marine diffusivity</td><td>K_m</td><td>m^2/yr</td><td colspan="3">200</td></tr>
<tr><td>Sand/shale ratio</td><td>F</td><td>-</td><td colspan="3">1</td></tr>
<tr><td>Sand/shale porosity</td><td>φ</td><td>-</td><td colspan="3">0</td></tr>
<tr><td>Sand/shale e-folding depth</td><td>z</td><td>m</td><td colspan="3">0</td></tr>
<tr><td>Depth averaging thickness</td><td>L</td><td>m</td><td colspan="3">100</td></tr>
<tr><td rowspan="2">Sediment rain</td><td rowspan="2">-</td><td rowspan="2">m/yr</td><td><10 Myr</td><td><20 Myr</td><td>Until model end</td></tr>
<tr><td>$1 \cdot 10^{-4}$</td><td>$5 \cdot 10^{-5}$</td><td>0</td></tr>
</table>

Table S2. Landscape evolution model parameters.

Model type	Kf ($m^{0.2}$ yr^{-1})	Phase 1	Phase 2		Phase 3		Phase 4		Phase 5
		start	start	duration (myr)	start	duration (myr)	start	duration (myr)	start
Asymmetric	0	0	<1	4	5	5	10	6	16
Asymmetric	1e-6	0	<1	6	7	4	11	24	35
Asymmetric	1e-5	0	<1	6	7	4	11	13	24
Asymmetric	1e-4	0	<1	9	10	3	13	20	33
Symmetric	0	0	<2	4	6	5	n/a		11
Symmetric	1e-6	0	<2	5	7	6	n/a		13
Symmetric	1e-5	0	<2	6	8	6	n/a		14
Symmetric	1e-4	0	<2	6	8	10	n/a		18
Wide	0	0	<1	13	15	5	n/a		20
Wide	1e-6	0	<1	18	20	4	n/a		24
Wide	1e-5	0	<1	18	20	4	n/a		24
Wide	1e-4	0	<1	22	23	8	n/a		28

Table S3. Table showing the phase timings for all models. The start subcolumn indicates the model time that a phase started at.

Movie S1. Model evolution of the medium surface process efficiency asymmetric rift model showing the upper 50 km of the tectonic model and the surface processes model. The surface processes model is exaggerated 3x in Z to better see the topography and is colored by the elevation (blue-green-white). The tectonic model shows the compositions with the upper crust (light gray), lower crust (dark gray), mantle lithosphere (blue), and the asthenosphere (light red). The sediment is colored by the depositional time in 5 Myr increments, and black contours show 2 Myr increments. Accumulated plastic strain is shown in opaque-black, and the strain rate in opaque-purple. White temperature contours are shown for temperatures of 200, 400, 600, and 800 C.

Movie S2. Model evolution of the medium surface process efficiency asymmetric rift model showing the upper 50 km of the tectonic model overlain by the extracted fault system. The model is colored by rheology, with sediment shown in tan and the strain rate in opaque-purple. The extracted fault network is colored by activity and fault orientation, with red (active left-dipping), blue (active right-dipping), and black (inactive) faults.White temperature contours are shown for temperatures of 200, 400, 600, and 800 C.

Movie S3. Model evolution of the medium surface process efficiency symmetric rift model showing the upper 50 km of the tectonic model and the surface processes model. The surface processes model is exaggerated 3x in Z to better see the topography and is colored by the elevation (blue-green-white). The tectonic model shows the compositions with the upper crust (light gray), lower crust (dark gray), mantle lithosphere (blue), and the asthenosphere (light red). The sediment is colored by the depositional time in 5 Myr increments, and black contours show 2 Myr increments. Accumulated plastic strain is shown in opaque-black, and the strain rate in opaque-purple. White temperature contours are shown for temperatures of 200, 400, 600, and 800 C.

Movie S4. Model evolution of the medium surface process efficiency symmetric rift model showing the upper 50 km of the tectonic model overlain by the extracted fault system. The model is colored by rheology, with sediment shown in tan and the strain rate in opaque-purple. The extracted fault network is colored by activity and fault orientation, with red (active left-dipping), blue (active right-dipping), and black (inactive) faults.White temperature contours are shown for temperatures of 200, 400, 600, and 800 C.

Movie S5. Model evolution of the medium surface process efficiency wide rift model showing the upper 50 km of the tectonic model and the surface processes model. The surface processes model is exaggerated 3x in Z to better see the topography and is colored by the elevation (blue-green-white). The tectonic model shows the compositions with the upper crust (light gray), lower crust (dark gray), mantle lithosphere (blue), and the asthenosphere (light red). The sediment is colored by the depositional time in 5 Myr increments, and black contours show 2 Myr increments. Accumulated plastic strain is shown in opaque-black, and the strain rate in opaque-purple. White temperature contours are shown for temperatures of 200, 400, 600, and 800 C.

Movie S6. Model evolution of the medium surface process efficiency wide rift model showing the upper 50 km of the tectonic model overlain by the extracted fault system. The model is colored by rheology, with sediment shown in tan and the strain rate in opaque-purple. The extracted fault network is colored by activity and fault orientation, with red (active left-dipping), blue (active right-dipping), and black (inactive) faults.White temperature contours are shown for temperatures of 200, 400, 600, and 800 C.